F. Topputo, Y. Wang, C. Giordano, V. Franzese, H. Goldberg, F. Perez-Lissi, R. Walker
Envelop of Reachable Asteroids by M-Argo Cubesat
Advances in Space Research, In press - Published online 05/03/2021
doi:10.1016/j.asr.2021.02.031

Envelop of reachable asteroids by M-ARGO CubeSat

Francesco Topputo[a,*], Yang Wang[a], Carmine Giordano[a], Vittorio Franzese[a], Hannah Goldberg[b], Franco Perez-Lissi[c], Roger Walker[c]

[a] *Politecnico di Milano, Dept. of Aerospace Science and Technology, Via La Masa 34, 20156, Milan, Italy*
[b] *GomSpace, Langagervej 6, 9220, Aalborg, Denmark*
[c] *European Space Research and Technology Centre, Keplerlaan 1, 2201, AZ Noordwijk, Netherlands*

Abstract

The Miniaturised Asteroid Remote Geophysical Observer (M-ARGO) is planned to be the first standalone deep-space CubeSat mission to rendezvous with and characterise a near-Earth asteroid. To this aim, it is essential to assess the attainable set of target asteroids. This work presents the initial results of the mission analysis and design of M-ARGO. In particular, the original procedure developed to extract the reachable near-Earth asteroids and the subsequent down-selection process are shown. Hundreds of both time- and fuel-optimal low-thrust trajectory optimisation problems have been solved with an indirect approach, targeting asteroids pre-filtered from the Minor Planet Center Database. The method implements a realistic thruster model, featuring variable input power, thrust, and specific impulse, together with an accurate switching detection technique and analytic derivatives. The analysis shows that approximately 150 minor bodies are found potentially reachable by M-ARGO when departing from the Sun–Earth Lagrange point L_2 within a 3-year transfer duration. A manual inspection of the transfer features led to a subset of 41 targets seeming more promising according to mission technological requirements and constraints. Initial results indicate mission feasibility for M-ARGO, which has the potential to enable a completely new class of low-cost deep-space exploration missions.

Keywords: M-ARGO, Deep-space CubeSats, Low-thrust trajectory, Near-Earth asteroids

*Corresponding author.
Email addresses: francesco.topputo@polimi.it (Francesco Topputo), yang.wang@polimi.it (Yang Wang), carmine.giordano@polimi.it (Carmine Giordano), vittorio.franzese@polimi.it (Vittorio Franzese), franco.perez.lissi@esa.int (Franco Perez-Lissi), roger.walker@esa.int (Roger Walker)

1. Introduction

The success of CubeSats spurred increasing interests towards nano-satellite missions (Poghosyan and Golkar, 2017). The low-cost nature of CubeSats allows small companies and universities to take part in space missions, expanding the access to space to a wider community. Nowadays, CubeSats have reduced the entry-level cost for space missions in Low Earth Orbit (LEO) by more than one order of magnitude (Walker et al., 2018). This is owing to the advances in miniaturized commercial-off-the-shelf components and to the short design-to-launch time. All in all, CubeSats as M-ARGO, have the potential to reduce the entry-level cost of interplanetary missions as well.

Deep-space CubeSats offer the possibility of augmenting and diversifying the Solar System exploration at a lower cost compared to traditional missions, thus providing high science-to-investment ratios. For instance, deep-space CubeSats would allow the characterization of several asteroids in the Solar System, so contributing tremendously to the understanding of its evolution.

MarCO, the first deep-space CubeSat mission, successfully performed a Mars fly-by, thus demonstrating the CubeSat technology for deep-space missions (Klesh and Krajewski, 2015; Schoolcraft et al., 2017). Following this trend, space agencies have supported several interplanetary CubeSat mission studies. The European Space Agency (ESA) has funded, among others, M-ARGO (Miniaturized Asteroid Remote Geophysical Observer) (Walker et al., 2018), LUMIO (Lunar Meteoroid Impacts Observer) (Franzese et al., 2019; Topputo et al., 2018b; Speretta et al., 2019; Cipriano et al., 2018), VMMO (Volatile and Mineralogy Mapping Orbiter) (Kruzelecky, 2018), and two CubeSats along the Hera mission (Michel et al., 2018), Milani (Ferrari et al., 2021) and Juventas (Goldberg et al., 2019). The National Aeronautics and Space Administration (NASA) has funded several nano-class deep-space missions along the Artemis-1 and Artemis-2 opportunities (McIntosh et al., 2020; Malphrus et al., 2020; Lockett et al., 2020), along with the Japan Aerospace Exploration Agency (JAXA) (Dei Tos and Baresi, 2020; Oguri et al., 2020).

Target selection is an essential task in the preliminary design of asteroid missions (Qiao et al., 2006; Peloni et al., 2016; Machuca et al., 2020; Wagner et al., 2015). In this context, the present work aims to find the reachable NEA targets considering the performances and constraints of M-ARGO mission. M-ARGO is proposed as the first ESA stand-alone CubeSat mission to rendezvous with and characterise a near-Earth asteroid (NEA) (Walker et al., 2017). M-ARGO is planned to be released around the second Sun–Earth Lagrangian point L_2. From this orbit, M-ARGO will make its own deep-space transfer to a designated

NEA target, thus demonstrating the capability of CubeSats to independently explore deep-space objects.

A preliminary work along these lines was conducted by ESA's Concurrent Design Facility (CDF). The present work is an enhancement of (Mereta and Izzo, 2018) with a more comprehensive and sophisticated target asteroid search. Specifically, a general and systematic target screening procedure for low-thrust asteroid missions is proposed. A realistic thruster model is incorporated into the optimization framework, featuring variable maximum thrust and specific impulse as a function of the input power, which in turn depends upon the spacecraft distance to the Sun. Both time-optimal and fuel-optimal solutions are obtained using the solver Low-Thrust Trajectory Optimiser (LT2.0) (Topputo et al., 2018a), which is an indirect optimization solver featuring analytic Jacobian and accurate solutions with bang-bang control structure. The time-optimal and fuel-optimal solutions compliant with the M-ARGO performances and constraints are collected and ranked, thus generating the reachable set of asteroids. The ranked lists are processed manually considering the search outcomes for each body. In turn, a subset of 41 targets is then defined, out of which a liberal choice of 5 short-listed targets is made. It is worth mentioning that the target screening exercise has to map the advancements in M-ARGO mission and system design. Therefore, the initial results presented in this paper might be subject to changes in later stages of the design. Yet, we believe that our study is useful for the minor body community as well as for other similar missions to follow in the future.

The paper is structured as follows. Section 2 presents an overview of the M-ARGO mission and summarizes the assumptions made for the platform. Section 3 shows the approach for the NEO targets screening. Section 4 details the asteroids database pre-filtering step. Then, the methodology and the results for the time-optimal and fuel-optimal transfers are shown in Section 5 and Section 6, respectively. The envelop of reachable targets is reported in Section 7. Conclusions are drawn in Section 8.

2. M-ARGO mission

M-ARGO is a 12U CubeSat that is planned to piggyback on the launch of another large spacecraft going towards the Sun–Earth Lagrange point L_2. After insertion into a parking orbit at L_2, M-ARGO will depart from there performing a deep-space cruise towards a NEA target using low-thrust electric propulsion. M-ARGO will perform an in-orbit demonstration of key technologies such as (Walker et al., 2018) i) a miniaturized X-band transponder and reflectarray high gain antenna for communication with Earth at distances

of up to 1.5 AU; ii) a miniaturized solar drive array mechanism for maximising solar power generation from two deployable steerable wings; iii) miniaturized electric propulsion for orbital manoeuvres.

The M-ARGO mission objectives are reported in Table 1. These are to: (1) demonstrate the capability of CubeSat nano-spacecraft systems to independently explore deep space for the first time; (2) rendezvous with a near-Earth asteroid and characterize its physical properties for the presence of in-situ resources; (3) advance miniaturized technologies currently under development in Europe; (4) test autonomous guidance, navigation, and control techniques and components performance during transfer to target object.

Table 1: M-ARGO mission objectives.

ID	Title	Statement
1	CubeSat Demonstration	Demonstrate the capability of CubeSat nano-spacecraft systems to independently explore deep space for the first time.
2	Scientific Investigation	Rendezvous with a near-Earth asteroid and characterize its physical properties for the presence of in-situ resources.
3	Technology Advancement	Advance miniaturized technologies currently under development in Europe.
4	Autonomy Experimentation	Test autonomous guidance, navigation, and control techniques and components performance during transfer to target object.

2.1. Mission and spacecraft data

M-ARGO is planned to depart from the Sun–Earth L_2 point within 1 Jan 2023 and 31 Dec 2024. The maximum transfer time to the asteroid is set to up to 3 years, and the close-proximity operations (CPO) are planned to last up to 6 months. The preliminary spacecraft mass amounts to $m_0 = 22.6$ kg, where $m_{p,\max} = 2.8$ kg is the maximum available propellant. The Sun-projected area for the computation of the solar radiation pressure is $A = 0.30$ m^2 with a reflectivity coefficient of ($C_r = 1.3$). These values are given in Table 2.

2.2. Thruster model

The mission analysis implements a realistic thruster model, that is, a model mapping maximum thrust and specific impulse variation over the instantaneous input power. The

Table 2: Mission time frame and spacecraft data assumptions.

S–E L_2 Departure	**Transfer**	**CPO**	m_0	$m_{p,\max}$	A	C_r
2023 – 2024	$\leq$ 3 years	$\leq$ 6 months	22.6 kg	2.8 kg	0.30 m^2	1.3

thruster model assumes that both the maximum thrust, $T_{\max}$, and the specific impulse, I_{sp}, depend on the instantaneous engine input power, P_{in}, which in turn is a function of the Sun distance, r. These functions have been handled using fourth-order polynomials, which represent surrogate models of the miniaturized ion thruster as well as the power production and distribution units to be used in M-ARGO. Fourth-order polynomials allow capturing the complexities of these systems when used in conjunction, while still assuring smooth, non-singular derivatives:

$$T_{\max} = a_0 + a_1 P_{in} + a_2 P_{in}^2 + a_3 P_{in}^3 + a_4 P_{in}^4 \quad (1)$$

$$I_{sp} = b_0 + b_1 P_{in} + b_2 P_{in}^2 + b_3 P_{in}^3 + b_4 P_{in}^4 \quad (2)$$

$$P_{in} = c_0 + c_1 r + c_2 r^2 + c_3 r^3 + c_4 r^4 \quad (3)$$

Beside the variation in Eq. (3), the thruster input power is bounded within a minimum and maximum value, $P_{\min} = 20$ W and $P_{\max} = 120$ W, respectively, for technological limits. Although the value of the 15 coefficients $\{a_i, b_i, c_i\}$, $i = 0, \ldots, 4$, in Eqs. (1)–(3) as well as those for $P_{\min}$ and $P_{\max}$ will be known with greater confidence in later stages of the design, the values used in this work are given in Table 3. Figure 1 shows the performances of the thruster model.

Table 3: Thruster model coefficients.

$T_{\max}$	Value	Unit	I_{sp}	Value	Unit	P_{in}	Value	Unit
a_0	-0.7253	mN	b_0	2652	s	c_0	840.11	W
a_1	0.02481	mN/W	b_1	-18.123	s/W	c_1	-1754.3	W/AU
a_2	0		b_2	0.3887	s/W^2	c_2	1625.01	W/AU^2
a_3	0		b_3	-0.00174	s/W^3	c_3	-739.87	W/AU^3
a_4	0		b_4	0		c_4	134.45	W/AU^4

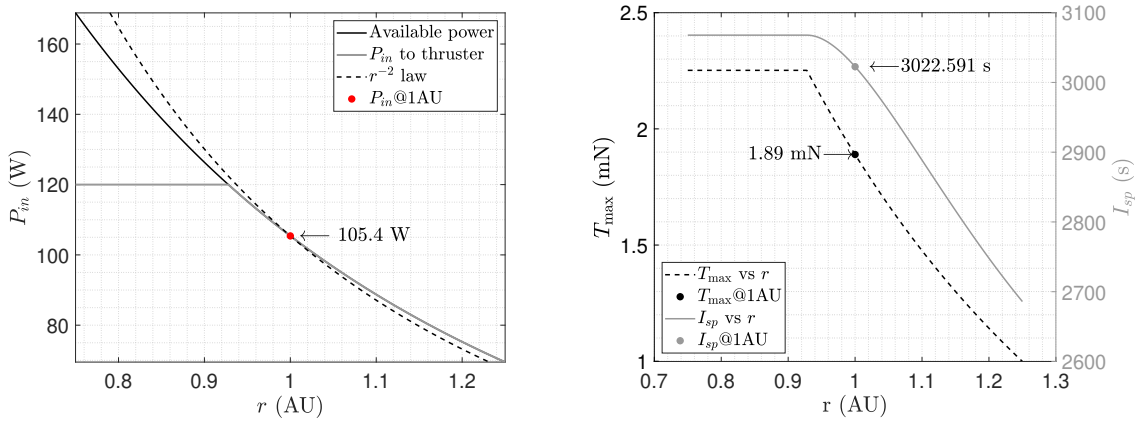

(a) P_{in} (light-gray continuous line) versus r

(b) $T_{\max}$ (dashed line) and I_{sp} (continuous line) versus r

Figure 1: Graphical representation of the thruster model used.

3. Approach to target selection

This section shows the approach undertaken to down-select the NEA targets for M-ARGO. To this aim, it is required to identify the subset of asteroids that are reachable considering the constraints of a 12U deep-space CubeSat. Figure 2 shows the procedure developed to filter the database of known asteroids.
The procedure is as follows:

1-2 **Database retrieval.** The Minor Planet Center (MPC) Database[1] is considered as the source of information for the minor planets in the Solar System. It comprehends the designation and the orbit computation of all the discovered minor planets and it is updated daily. More than $900,000$ objects are accounted for as of October 2020.

3-4 **Pre-Filtering.** The full list of asteroids is pre-filtered using ranges of orbital parameters. Educated guesses on these parameters have been inferred from (Mereta and Izzo, 2018). These involve capping the aphelion, bottoming the perihelion, and bounding the inclination as well as the number of observations. This filtering reduces the full list of asteroids to a preliminary list of approximately 500 potential targets; see Section 4.

5-6 **Time-optimal transfers.** A massive search is conducted to compute time-optimal

[1]See `https://minorplanetcenter.net/`; last accessed on October 2020.

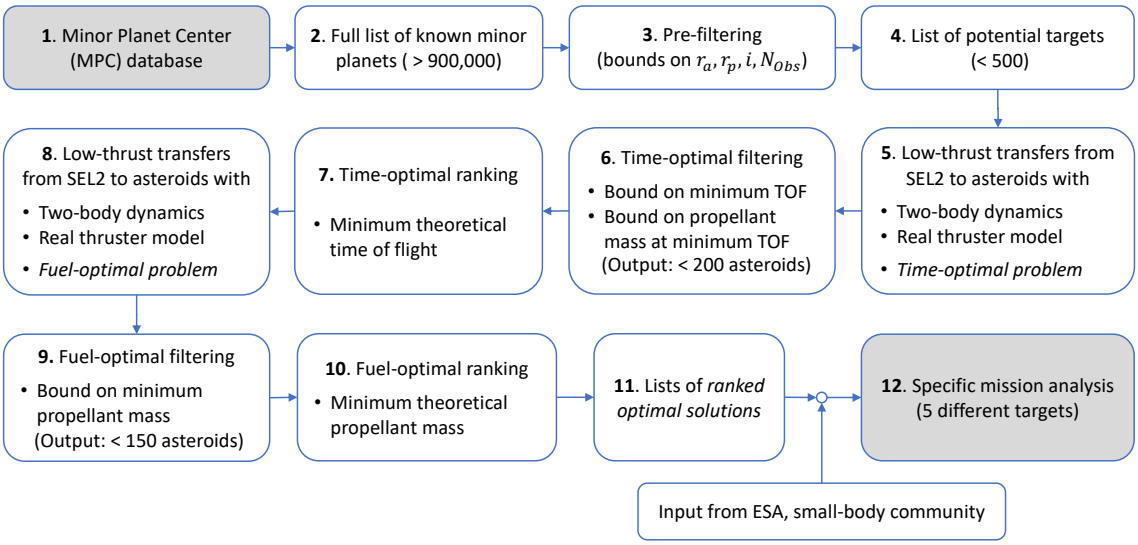

Figure 2: Methodology of the NEO target screening.

transfers to each of the asteroids in the preliminary list. The optimisation considers the two-body problem with the realistic thruster model in Section 2.2, departure from Sun–Earth L_2, and departure window as specified in Section 2.1. The aim of this step is to determine the *minimum theoretical transfer time* to each asteroid for each departure epoch. The targets whose minimum transfer time is greater than 900 days are filtered-out.

7 **Time-optimal ranking.** The filtered time-optimal solutions are ordered to produce a time-optimal ranking. The number of targets is then reduced to $\sim$ 170 objects; see Section 5.

8-9 **Fuel-optimal transfers.** The objects resulting feasible after the time-optimal analysis are processed under the perspective of a fuel-optimal optimisation, using the same model and boundary conditions as in the time-optimal optimisation. This analysis finds the minimum propellant mass for each combination of departure epoch and transfer time. The targets whose minimum required propellant mass is greater than 2.8 kg are excluded from the list.

10 **Fuel-optimal ranking.** The fuel-optimal solutions as output of step 9 are ordered to produce a fuel-optimal ranking made of approximately 150 reachable objects; see Section 6.

Table 4: Asteroids data sources.

Source	Acronym	Type	Data
Minor Planet Center[2]	MPC	Database	Asteroids Orbital Parameters
Asteroid Lightcurve[3]	LCDB	Database	Asteroids Physical Data
HORIZONS[4]	HORIZONS	SPICE Kernels	Asteroids Ephemerides

11 **Lists of ranked optimal solutions.** The ranked lists of time-optimal and fuel-optimal solutions produced as output of the filtering chain has been examined in view of operational and scientific criteria; see Section 7. The 5 shortlisted targets have been then selected; see Section **??**.

4. Database filtering

The Minor Planet Center (Table 4) accounts for more than 900,000 objects in the Solar System. Figure 3a shows the semi-major axis (a) versus the eccentricity (e) for all the near-Earth asteroids as a scatter plot, while Figure 3b displays the semi-major axis (a) versus the inclination (i) for the same bodies.

Consistently with the preliminary work in (Mereta and Izzo, 2018), the subset of potential targets has been defined by restricting the aphelion (r_a) upper bound (UB) to 1.25 AU and the perihelion (r_p) lower bound (LB) to 0.75 AU. Moreover, in order to comply with realistic CubeSat propulsive capabilities, an upper bound on the inclination equal to 10 degrees has been set. Higher inclinations are unlikely to be reached due to the limited amount of propellant available. This is confirmed by the outcome of the analysis (see Section 6). Eventually, a lower bound of 10 observations (N_{obs}) is enforced to assure accuracy in the orbital elements of the asteroids. Table 5 summarises the filtering parameters used. It is worth highlighting that the intervals considered in this study are larger than those in (Mereta and Izzo, 2018): this choice is to perform a more comprehensive search not influenced by existing results. As a result, 456 objects satisfy the bounds in Table 5. These have been represented as black dots in Figure 3.

Figure 4 shows the estimated diameter (D) of the minor planets with respect to their

[2]See `https://minorplanetcenter.net/`

[3]See `http://www.minorplanet.info/lightcurvedatabase.html`

[4]See `https://ssd.jpl.nasa.gov/?horizons`

Table 5: NEA database filtering parameters.

Parameter	Lower Bound	Upper Bound
r_a	–	1.25 AU
r_p	0.75 AU	–
i	0 deg	10 deg
N_{obs}	10	–

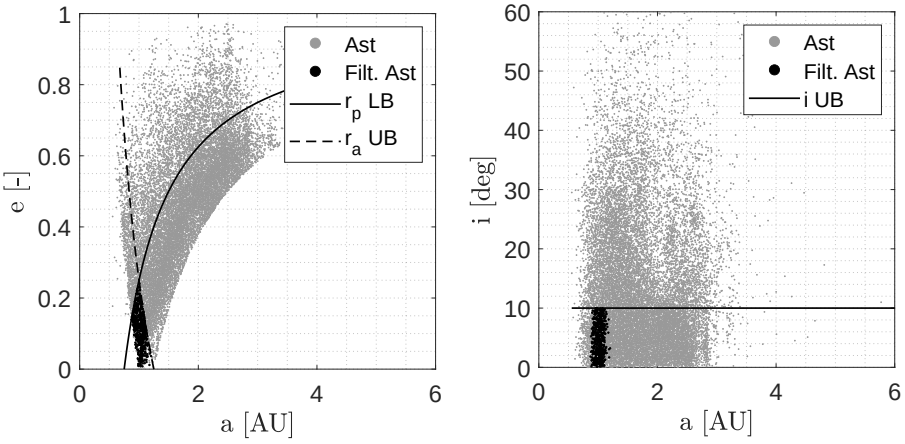

(a) a vs e (b) a vs i

Figure 3: Minor planets semi-major axis (a), eccentricity (e), and inclination (i). The filtering bounds are the solid and dashed lines, while the filtered asteroids are highlighted in black.

semimajor axis (a), eccentricity (e), and inclination (i). In Fig. 4, the diameter D is estimated as[5] (Bowell et al., 1989; Harris, 1997)

$$D = 10^{3.1236 - 0.5 \log_{10}(a_L) - 0.2H} \tag{4}$$

where H is absolute magnitude and a_L is albedo, whose values are retrieved from the databases in Table 4. The filtered asteroids are highlighted as black dots. The diameter of the filtered asteroids ranges between 10^{-3} and 10^{-1} km.

Figure 5 shows the estimated size versus the rotational period of the asteroids catalogued in the Asteroid Lightcurve Database (LCDB) (Warner et al., 2009); see Table 4. The plot

[5]See `https://cneos.jpl.nasa.gov/tools/ast_size_est.html`

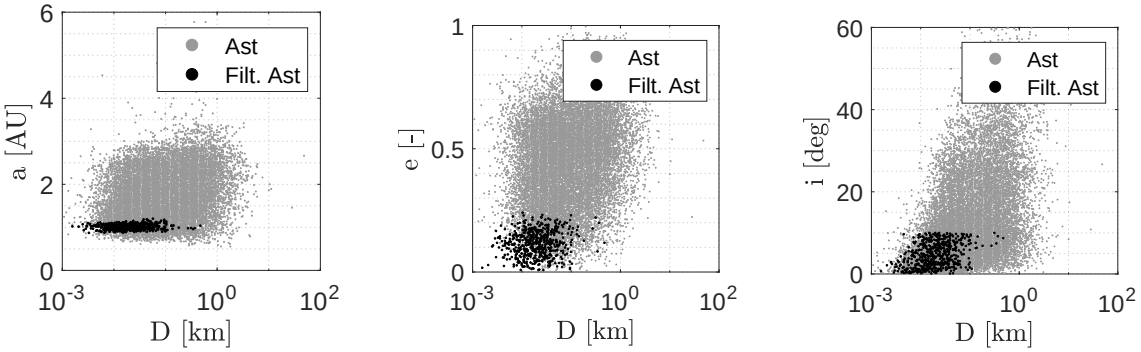

(a) D vs a (b) D vs e (c) D vs i

Figure 4: Minor planets diameter (D) versus semi-major axis (a), eccentricity (e), and inclination (i). Filtered asteroids are the black dots.

highlights the so called spin barrier (horizontal dashed line). Most of the big asteroids (with a diameter larger than 1 km) lie below the spin barrier, meaning that they have a rotational period higher than 2 hours, while for small asteroids the rotational period can be small, in the order of 1 hour or less. The filtered asteroids for which light curves are known are also highlighted in black in Fig. 5.

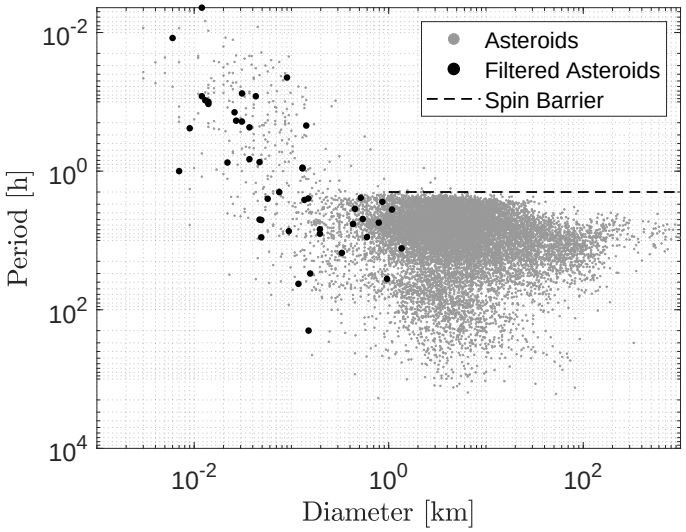

Figure 5: Rotational period against diameter for minor planets. Filtered asteroids in black. Data retrieved from the MPC and the LCDB; see Table 4. The U code defined in the LCDB database provides a measure of the quality of the period solution. Only asteroids with $U \geq 2$ are illustrated.

5. Time-optimal transfers

Performing a time-optimal search in a two-year departure window for different objects requires solving approximately 3.3×10^5 optimisation problems with a one-day time discretisation. The indirect solver LT2.0 (Low-Thrust Trajectory Optimiser 2.0) internally developed at Politecnico di Milano (Topputo et al., 2018a) has been adapted for this purpose. The dynamic model used is a standard two-body problem implementing the realistic thruster model in Section 2.2. Second-order effects such as third-body perturbation and solar radiation pressure have been implemented in following phases of the mission analysis.

5.1. Methodology for time-optimal solutions

An indirect approach is chosen to solve a myriad of optimal control problems in an efficient way. The essence is using the first-order necessary conditions to state a two-point boundary value problem (TPBVP) and the associated shooting function (Bryson and Ho, 1975). A zero-finding problem is then employed to solve for the initial costate. While a detailed derivation can be found in, e.g., Russell (2007), this section, as well as Section 6.1, recalls the basics of the indirect approach used, which is based on Zhang et al. (2015).

The time-optimal transfers for the filtered asteroids in Section 4 are solved with the departure window in Table 2. The Sun-centered two-body problem is employed. Numerical experiments show that solutions continued in higher fidelity models, which consider the gravitational acceleration of the Sun and the planets, the solar radiation pressure, and the non-spherical gravity, feature negligible differences from those found in this model. Indeed, an average increase of 5% in propellant mass is found, mainly to counteract the gravitational acceleration of the Earth, when the spacecraft is close to L_2. The dynamics in ecliptic J2000 frame read

$$\begin{cases} \dot{\boldsymbol{r}} = \boldsymbol{v} \\ \dot{\boldsymbol{v}} = -\dfrac{\mu}{r^3}\boldsymbol{r} + u\dfrac{T_{\max}}{m}\boldsymbol{\alpha} \\ \dot{m} = -u\dfrac{T_{\max}}{I_{sp}\, g_0} \end{cases} \tag{5}$$

where $\boldsymbol{r}$, $\boldsymbol{v}$, and m are the spacecraft position vector, velocity vector, and mass, respectively, while $u \in [0, 1]$ is the throttle factor and $\boldsymbol{\alpha}$ is the thrust pointing unit vector; g_0 is the gravitational acceleration at sea level.

The initial time, t_0, is assumed to be any epoch in the departure window. The initial

condition is

$$\boldsymbol{r}(t_0) - \boldsymbol{r}_0 = 0, \quad \boldsymbol{v}(t_0) - \boldsymbol{v}_0 = 0, \quad m(t_0) - m_0 = 0 \tag{6}$$

where $\boldsymbol{r}_0$ and $\boldsymbol{v}_0$ are the heliocentric position and velocity vectors as given by the DE451 model for the Sun–Earth L_2 SPICE kernel[6] (Acton et al., 2018); see Table 4. The kernel allows extracting position and velocity vectors as function of the departure epoch t_0; m_0 is instead the spacecraft mass as specified in Table 2.

Consistently with the thruster model in Section 2.2, we have assumed that both the maximum thrust, $T_{\max}$, and the specific impulse, I_{sp}, in Eq. (5) vary with the engine input power P_{in}, which is in turn function of the Sun distance.

In the time-optimal problem, we want to rendezvous with a moving target. Therefore, the final time, t_f, and consequently the final mass, $m(t_f)$, are both free. The final, rendezvous conditions are therefore

$$\boldsymbol{r}(t_f) - \boldsymbol{r}_t(t_f) = 0, \quad \boldsymbol{v}(t_f) - \boldsymbol{v}_t(t_f) = 0 \tag{7}$$

where $\boldsymbol{r}_t(t)$ and $\boldsymbol{v}_t(t)$ are the position and velocity vectors of the target body, respectively. These two functions have been retrieved from the objects' SPICE kernels from HORIZONS system (Giorgini and Yeomans, 1999).

The objective function is

$$J = \int_{t_0}^{t_f} 1 \, \mathrm{d}t \tag{8}$$

thus the Hamiltonian reads

$$H_t = \boldsymbol{\lambda}_r \cdot \boldsymbol{v} + \boldsymbol{\lambda}_v \cdot \left(-\frac{\mu}{r^3}\boldsymbol{r} + u\frac{T_{\max}}{m}\boldsymbol{\alpha} \right) - \lambda_m u \frac{T_{\max}}{I_{sp}\, g_0} + 1 \tag{9}$$

The thrust pointing angle is such that H_t is minimised at any time by virtue of the Pontryagin minimum principle (PMP) (Zhang et al., 2015)

$$\boldsymbol{\alpha}^*(t) = -\frac{\boldsymbol{\lambda}_v}{\lambda_v} \tag{10}$$

The thrust pointing angle is implicitly determined by the Lagrange multiplier $\boldsymbol{\lambda}_v$. The

[6] See `https://naif.jpl.nasa.gov/pub/naif/generic_kernels/spk/lagrange_point/` (Last access on December 2020). The Lagrange points kernels were generated by Min-Kun Chung of the Navigation and Mission Design Section at JPL.

optimal thrust throttle u^* satisfies

$$u^* = \begin{cases} 0 & \text{if } S_t > 0 \text{ or } P_{in} < P_{\min} \\ 1 & \text{if } S_t < 0 \text{ and } P_{in} \geq P_{\min} \\ \in [0,1] & \text{if } S_t = 0 \text{ and } P_{in} \geq P_{\min} \end{cases} \tag{11}$$

where the time-optimal switching function S_t is

$$S_t = -\lambda_m - \frac{I_{sp}\, g_0}{m} \lambda_v \tag{12}$$

Since optimal solutions satisfy $\lambda_m(t_f) = 0$ and $\dot{\lambda}_m \leq 0$, then $S_t < 0$. Moreover, $P_{in} \geq P_{\min}$ always (see Fig. 1a bearing in mind that $P_{\min} = 20$ W). Thus, $u^* = 1$ at all times.
The problem is to find $\{\boldsymbol{\lambda}_0, t_f\}$ that allow integrating Eq. (5) and the costate dynamics (not reported for brevity sake), with the initial conditions in Eq. (6) and the implicit control policy in Eqs. (10)–(11) such that the solution zeroes the shooting function

$$\boldsymbol{\Gamma}_t(\boldsymbol{\lambda}_0, t_f) = \begin{pmatrix} \boldsymbol{r}(t_f) - \boldsymbol{r}_t(t_f) \\ \boldsymbol{v}(t_f) - \boldsymbol{v}_t(t_f) \\ \lambda_m(t_f) \\ H(t_f) - \boldsymbol{\lambda}_r(t_f) \cdot \boldsymbol{v}_t(t_f) - \boldsymbol{\lambda}_v(t_f) \cdot \boldsymbol{a}_t(t_f) \end{pmatrix} \tag{13}$$

where $\boldsymbol{a}_t = \dot{\boldsymbol{v}}_t$.
Reconstructing the time-optimal transfers for 456 objects over a two-year departure window requires solving approximately 3.3×10^5 time-optimal problems. Thus, an agile strategy has been developed to scan the solution space.

5.2. Continuation of time-optimal solutions

The continuation strategy illustrated in Fig. 6 to scan the two-year window is employed to reduce computational load. Specifically, the time-optimal solution for a given t_0 is found first. Then, the solution for $t_0 + \Delta t$ is sought, using the optimal solution of the former step (t_0) as initial guess, with $\Delta t = 1$ day. If a new solution is found, the continuation proceeds. Otherwise, the time step Δt is halved. This process is repeated until the final departure date is reached. Consequently, the two-year window is processed with a nonuniform discretisation. The initial guess solution to the first problem is generated us-

ing the Adjoint Control Transformation (ACT) (Russell, 2007), along with a monotonically increasing transfer duration guess.

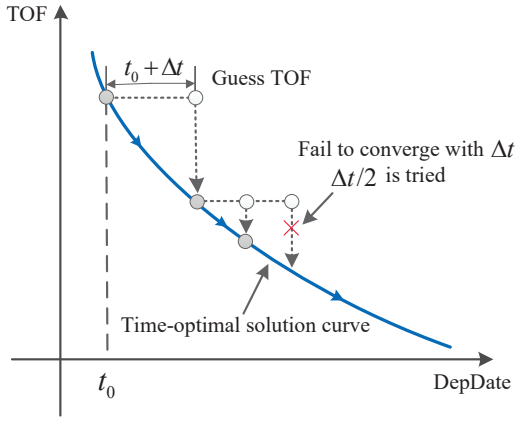

Figure 6: The continuation strategy to solve time-optimal transfers within the two-year departure window.

While these solutions are not feasible in practical applications, because they involve thrust on for all times, they yield the minimum theoretical transfer time

$$\tau_{\min} = \min_{t_0 \in [\underline{t}_0, \bar{t}_0]} \tau(t_0) \tag{14}$$

where $\tau(t_0) := t_f(t_0) - t_0$, and $[\underline{t}_0, \bar{t}_0]$ is the two-year departure window. $\tau_{\min}$ is used to prune out those solutions not complying with the requirement in Table 2.
The results of the time-optimal search for four sample asteroids are shown in Fig. 7, where the minimum transfer duration $\tau = t_f - t_0$ (left y-axis) and its associated propellant mass $m_p(\tau)$ (right y-axis) profiles are shown as function of the departure day t_0 (in MJD2000[7]). It can be seen that there are considerable variations of the transfer time in the two-year window. The minima of the transfer time corresponds to minima of the propellant mass because the thrust is always on.

5.3. Search space pruning

For each of the asteroids processed, $\tau_{\min}$ is retrieved, as well as its corresponding propellant mass $m_p(\tau_{\min})$. The two quantities are reported in Fig. 8 in the form of cumulative

[7] Julian Date is the interval of time measured in days from the epoch Jan 1, 4713 B.C., 12:00. Modified Julian Date (MJD2000) is the adjustment of Julian Date from Jan 1, 2000, 12:00 (Vallado, 2013).

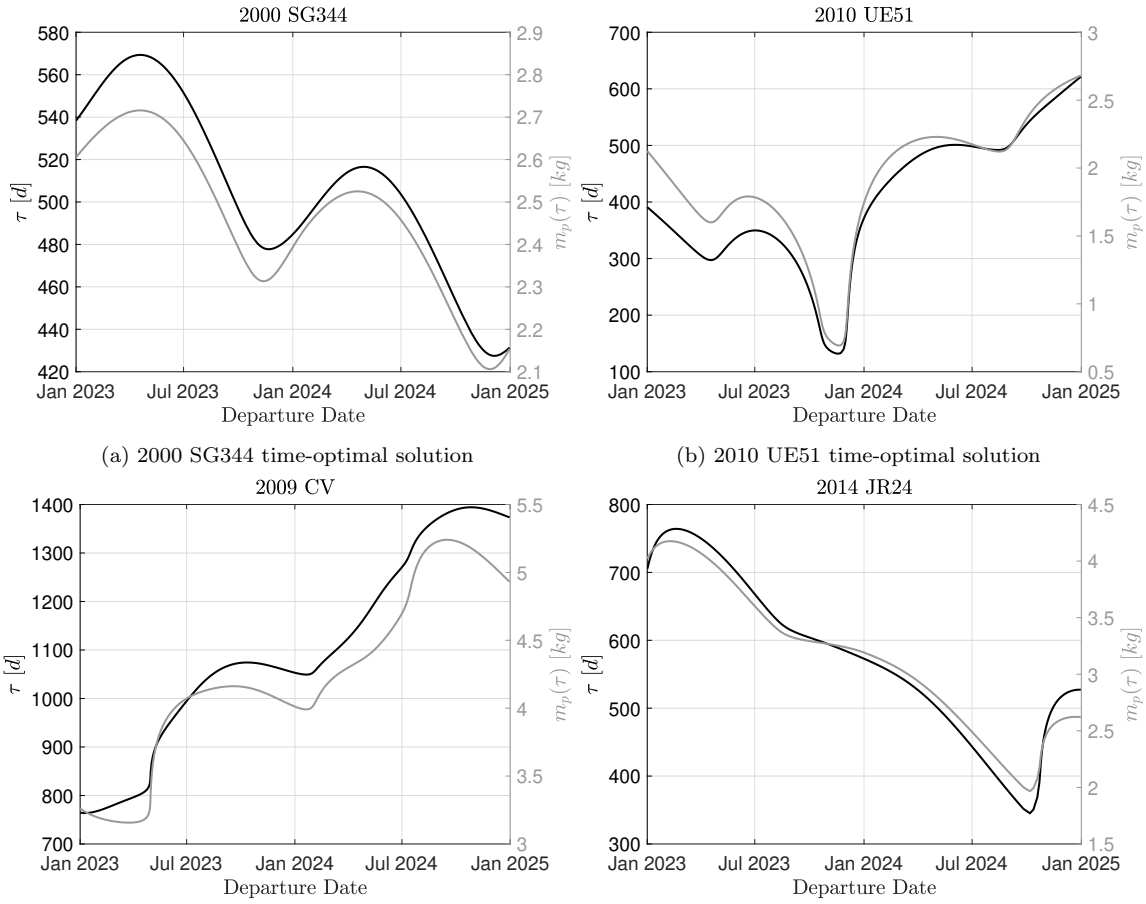

(a) 2000 SG344 time-optimal solution

(b) 2010 UE51 time-optimal solution

(c) 2009 CV time-optimal solution

(d) 2014 JR24 time-optimal solution

Figure 7: Minimum transfer time τ and associated propellant mass $m_p(\tau)$ profiles as function of the departure day for four sample asteroids.

distribution functions. This information has been used to further narrow the set of asteroids that can be reached by M-ARGO. Indeed, using the requirements in Table 2, and considering that the *real* transfer time is longer than the one resulting from time-optimal computations, the following criteria have been used.

1) Minimum theoretical transfer time lower than 900 days: $\tau_{\min} \leq 900$ days. There are 299 asteroids out of the ones processed satisfying this condition; see Fig. 8a.

2) Minimum propellant mass lower than 4 kg: $m_p(\tau_{\min}) \leq 4$ kg. There are 181 asteroids out of the one processed whose minimum propellant mass is below this threshold; see

Fig. 8b.

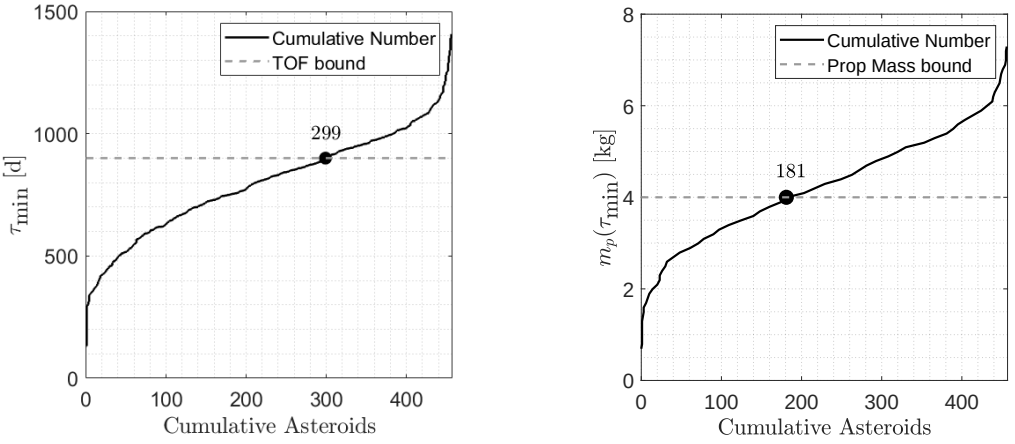

(a) Cumulative number of asteroids vs $\tau_{\min}$

(b) Cumulative number of asteroids vs $m_p(\tau_{\min})$

Figure 8: Cumulative number of asteroids for increasing $\tau_{\min}$ and associated $m_p(\tau_{\min})$. The filtering bounds are the dashed lines, while the number indicates the asteroids below the threshold.

We further impose that these two conditions have to be verified simultaneously. The graphical representation in Fig. 9 shows that the propellant mass condition is the more stringent one. As a result of this pruning process, we have 172 asteroids ranked after the time-optimal screening. The ranking is reported in Appendix A, and it is the input of the fuel-optimal step as per the approach in Fig. 2.

Inspection of Fig. 9 reveals that the points therein are the solution of the following differential equation

$$\dot{m} = -\frac{T_{\max}(P_{in}(t))}{g_0\, I_{sp}(P_{in}(t))} \tag{15}$$

because $u(t) = 1\ \forall t \in [t_0, t_f]$. Differently from the standard cases in which $T_{\max}$ and I_{sp} are both constant, Eq. (15) cannot be solved in closed form because $P_{in} = P_{in}(r(t))$. However, it is easy to verify that $T_{\max}(P_{in}(t))/I_{sp}(P_{in}(t))$ is monotonously increasing w.r.t. P_{in}. Thus, transfers to inner and outer targets (where inner and outer is referred to the Earth orbit) are bounded by $P_{in}(t) = P_{\max}$ and $P_{in}(t) = P_{\min}$, respectively. These conditions define the limiting minimum time to reach inner and outer targets, i.e.,

$$\tau_{\min,\text{in}} = \frac{g_0\, I_{sp}(P_{\max})}{T_{\max}(P_{\max})} m_p \tag{16}$$

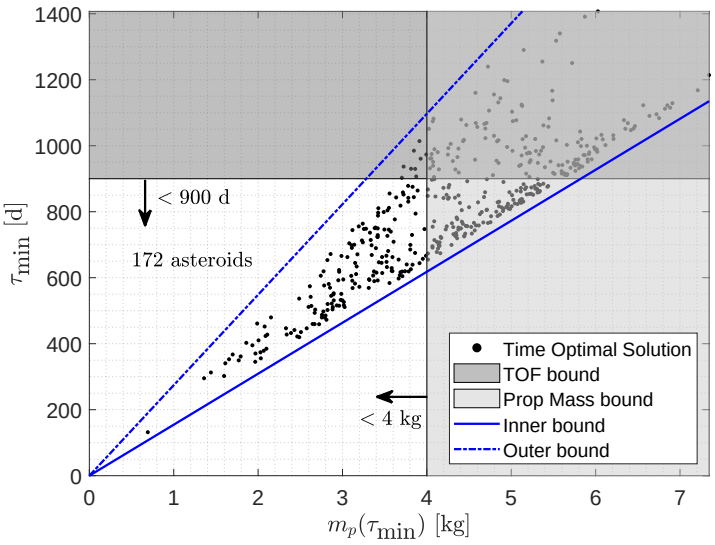

Figure 9: Time of flight for the time-optimal solutions against the associated propellant mass. The filtering bounds are the black solid lines, while the number indicates the asteroids below both thresholds. All time-optimal solutions lie within the inner and outer lines.

$$\tau_{\min,\text{out}} = \frac{g_0 \, I_{sp}(P_{\min})}{T_{\max}(P_{\min})} m_p \tag{17}$$

which correspond to the two blue lines in Fig. 9. Note that $P_{\min} = 75$ W is considered in the outer line in Fig. 9, since this is approximately the minimum power found in the time-optimal screening. We can infer the following:

- For a given propellant mass, inner targets need shorter times than outer ones;
- For a given transfer time, outer targets need less propellant than inner ones.

6. Fuel-optimal transfers

The 172 potential targets that passed the time-optimal pruning are then processed under the perspective of a fuel-optimal step. It is worth highlighting that the fuel-optimal process widens the variable space as both the departure epoch t_0 and the time of flight TOF are let to vary. That is, while time-optimal problems have a one-dimensional search space (t_0), the fuel-optimal problems have a two-dimensional search space: [t_0, TOF]. A two-dimensional

grid is therefore used to construct pork chop plots[8].

6.1. Methodology for fuel-optimal solutions

The minimum-fuel optimization has been performed by using the same model as in the minimum-time optimization, Eq. (5). The boundary conditions are those in Eqs. (6) and (7). The objective function is the propellant mass used in the transfer

$$J = \int_{t_0}^{t_f} u \frac{T_{\max}}{I_{sp}\, g_0}\, \mathrm{d}t \tag{18}$$

With a two-dimensional search space, the propellant mass varies for any combination of t_0 and TOF. The Hamiltonian of the problem is

$$H = \boldsymbol{\lambda}_r \cdot \boldsymbol{v} + \boldsymbol{\lambda}_v \cdot \left(-\frac{\mu}{r^3}\boldsymbol{r} + u\frac{T_{\max}}{m}\boldsymbol{\alpha} \right) + \lambda_m \left(-u\frac{T_{\max}}{I_{sp}\, g_0} \right) + u\frac{T_{\max}}{I_{sp}\, g_0} \tag{19}$$

whose minimization (by virtue of the PMP) yields once again the thrust pointing law as in Eq. (10) and the following throttling law

$$u^* = \begin{cases} 0 & \text{if } S_f > 0 \;\text{ or }\; P_{in} < P_{\min} \\ 1 & \text{if } S_f < 0 \text{ and } P_{in} \geq P_{\min} \\ \in [0,1] & \text{if } S_f = 0 \text{ and } P_{in} \geq P_{\min} \end{cases} \tag{20}$$

where the fuel-optimal switching function, S_f, is

$$S_f = 1 - \lambda_m - \frac{I_{sp}\, g_0}{m}\lambda_v \tag{21}$$

The problem is to find $\boldsymbol{\lambda}_0$ that allows integrating Eq. (5) and the costate equations (not shown for brevity), with the initial conditions (6) and the implicit control structure in Eq. (10) and (20) such that the solution zeroes the shooting function

$$\boldsymbol{\Gamma}(\boldsymbol{\lambda}_0) = \begin{pmatrix} \boldsymbol{r}(t_f) - \boldsymbol{r}_f \\ \boldsymbol{v}(t_f) - \boldsymbol{v}_f \\ \lambda_m(t_f) \end{pmatrix} \tag{22}$$

[8] In practice, the search space of fuel-optimal transfers is three-dimensional because there is an homotopy parameter that is used to map energy-optimal problems into fuel-optimal problems (Zhang et al., 2015).

6.2. Continuation of fuel-optimal solutions

Figure 10 shows the continuation strategy used for the fuel-optimal transfers. For each departure day t_0, the time of flight TOF is bottomed by the corresponding minimum transfer time $\tau(t_0)$ (blue lines in Fig. 10) and capped by $\overline{\tau}$, the 3-year condition in Table 2. This variable range has been discretised using a nonuniform grid, to ease efficiency. Specifically, the time-optimal solution is retrieved for each departure date t_0. From this point, the search continues along vertical lines (see Fig. 10). Suppose that the solution for a given pair $\{t_0, \text{TOF}\}$ is found; then, the fuel-optimal solution for $\{t_0, \text{TOF} + \Delta\tau\}$ is sought using the previous solution as initial guess, with $\Delta\tau = 15$ days. If a new solution is found, the scanning proceeds. Otherwise, the time step $\Delta\tau$ is halved. This process is repeated until the maximum TOF is reached.

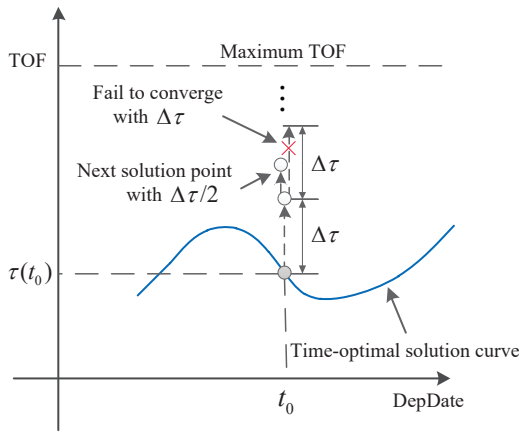

Figure 10: The continuation strategy to solve fuel-optimal transfers for the two-year departure window.

The outcome porkchop plots are shown for four sample targets in Fig. 11, where the same asteroids as in Fig. 7 have been used for consistency. The departure day (t_0) is on the x-axis, whereas the TOF is on the y-axis; the color code indicates the propellant mass m_p for each combination of (t_0, TOF). The red thick lines are the minimum-time profiles, and correspond to the dark lines in Fig. 7. The dashed region below the red line is therefore unfeasible: for a given departure date, M-ARGO can not take shorter than the corresponding point on the red line.

A number of optimal solutions are sampled arbitrarily from the plot of asteroid 2000 SG344 in Fig. 12. The points are labelled A–I, and the corresponding coordinates are given in Table 6. This exercise is performed to reveal the structure of the solutions inherent in the porkchop plots. Note that the samples are evenly spaced in terms of departure epoch

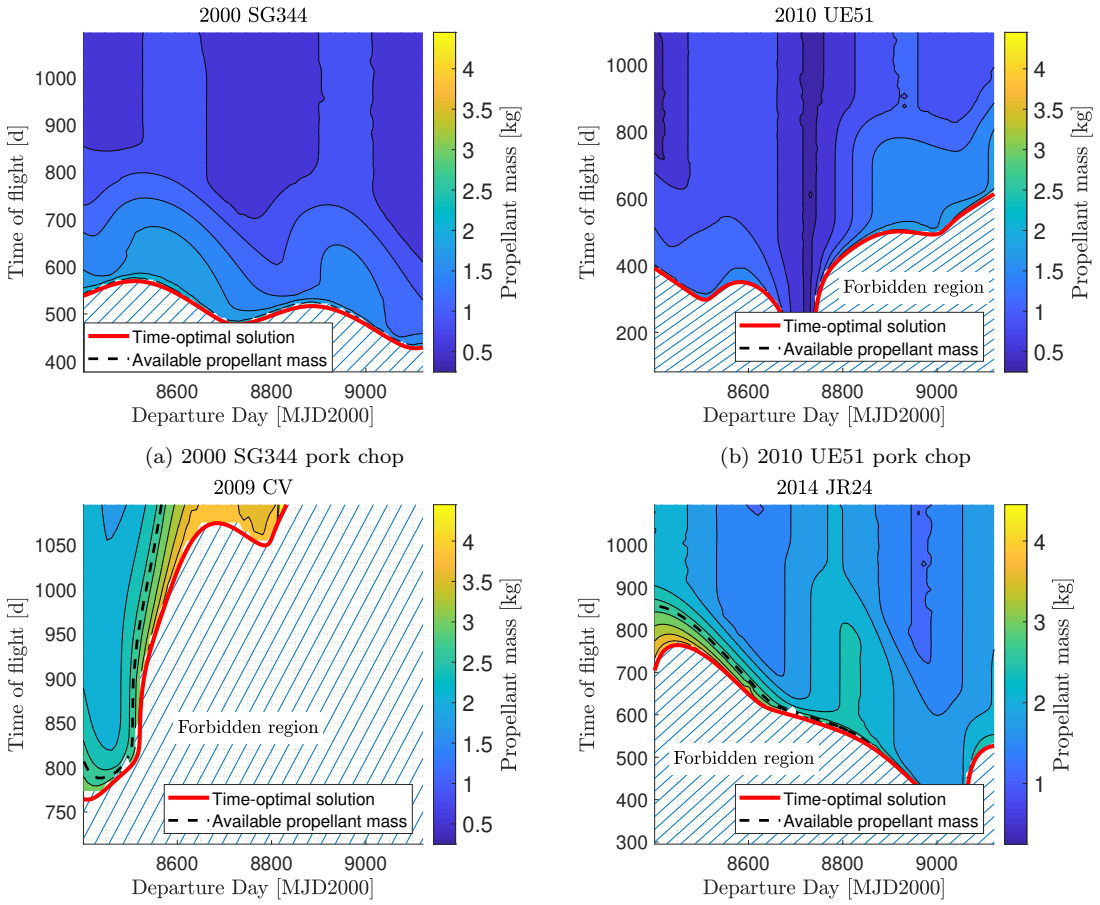

(a) 2000 SG344 pork chop

(b) 2010 UE51 pork chop

(c) 2009 CV pork chop

(d) 2014 JR24 pork chop

Figure 11: Pork chop plots for some sample asteroids. The available propellant mass ($m_{p,\max} = 2.8$ kg) is indicated with a black dashed line, while the red thick line shows the time-optimal solution. The color code is the propellant mass used, see the bars on the right.

and transfer time, except for A, D, and G that correspond to time-optimal solutions. The solutions that correspond to each of the nine points are reported in Figs. 13–15. In these figures, the following subfigures are given: Left: transfer trajectory in heliocentric frame (red: thrust arc, blue: coast arc); Center: throttle factor $u(t)$, switching function $S(t)$ ($S(t) = S_t(t)$ for time-optimal problems and $S(t) = S_f(t)$ for fuel-optimal problems), and spacecraft mass $m(t)$ profiles; Right: thruster input power $P_{in}(t)$, specific impulse $I_{sp}(t)$, and maximum thrust $T_{\max}(t)$ profiles.

Table 6: Coordinates of the samples in Fig. 12. The values of t_0 are in MJD2000.

Point	t_0	TOF [d]	**Point**	t_0	TOF [d]	**Point**	t_0	TOF [d]
A	8600	$\tau(t_0)$	D	8800	$\tau(t_0)$	G	9000	$\tau(t_0)$
B	8600	700	E	8800	700	H	9000	700
C	8600	900	F	8800	900	I	9000	900

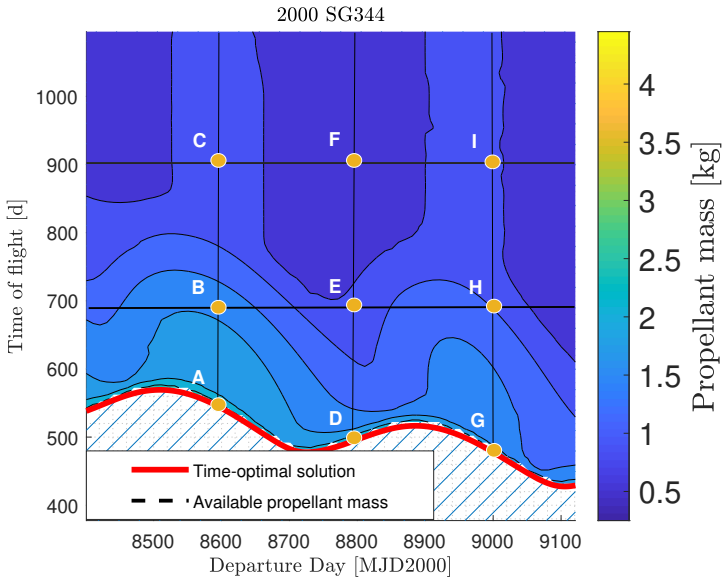

Figure 12: Pork chop plot for 2000 SG344 with sample points.

From Figs. 13–15 we can infer that: (1) the time-optimal solutions (A, D, G) have always thrust on ($u = 1$) as predicted by the theory; (2) the longer the transfer time, the higher the final mass, and therefore the lower the propellant used (this trend is reflected in different

shades of blue in Fig. 12, though it is not always valid); (3) there is a 10–15% variability of I_{sp} and 40–80% variability of $T_{\max}$ during the transfer, due to the variable P_{in}.

6.3. Search space pruning

For each target, worth to extract is the global minimum of the propellant mass, that is

$$m_{p,\min} = \min_{\substack{t_0 \in [\underline{t}_0, \bar{t}_0] \\ \mathrm{TOF} \in [\tau(t_0), \bar{\tau}]}} m_p(t_0, \mathrm{TOF}) \tag{23}$$

Graphically, $m_{p,\min}$ is the blue-most point in the pork chop plots. For the 172 asteroid processed, $m_{p,\min}$ is retrieved, as well as the corresponding value of t_0 and TOF. The global minimum propellant mass $m_{p,\min}$ is shown in the form of a cumulative distribution function in Fig. 16. This information has been used to further reduce the search space by enforcing the maximum propellant mass requirement in Table 2. It can be seen that 148 asteroids result feasible when enforcing this requirement. The list of these 148 asteroids is reported in Appendix B where they are ranked in terms of the global minimum propellant mass.

7. Target down-selection

With reference to the procedure developed for the NEO target screening, out of more than 900,000 minor bodies in the MPC database, 456 objects passed the pre-filtering, which was based on simple geometrical criteria. For these 456 objects, a minimum-time optimisation was carried out, and a subset made of 172 targets passed the pruning process when enforcing both a transfer time and a propellant mass thresholds (Section 5). These asteroids were then processed under the perspective of a minimum-fuel optimisation, and a subset of them made of 148 reachable targets was found (Section 6).

The whole process undertaken as well as the intermediate results are summarised in Table 7 (steps #1–#4). The focus is now on reducing further the set of reachable targets by pruning out those ones associated to transfers that are not desirable from the mission design point of view. This has been done through a one-by-one inspection of the porkchop plots, and yields a subset of downselected asteroids (step #5 in Table 7).

The pork chop plots related to the 148 reachable targets are reported in Appendix C. These figures embed relevant information, and their close-up analysis suggests that some targets might be more desirable than others in the time frame under consideration. Indeed, the following *qualitative* filtering criteria have been used:

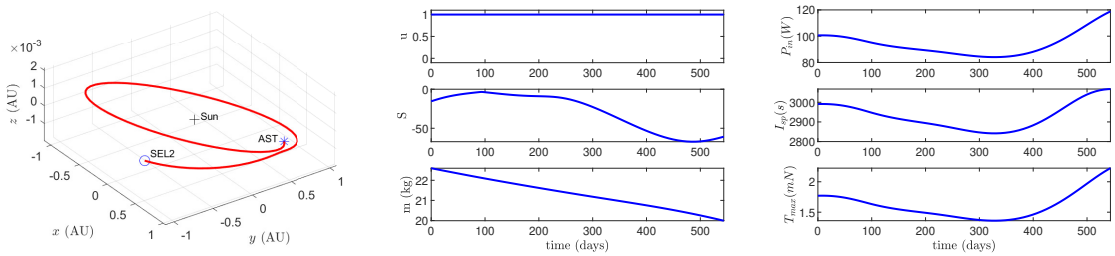

(a) Solution corresponding to point A in Fig. 12 (left: transfer trajectory; center: u, S, m; right: P_{in}, I_{sp}, $T_{\max}$).

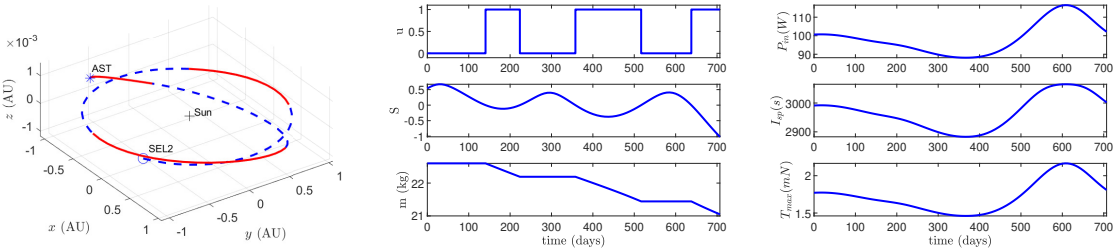

(b) Solution corresponding to point B in Fig. 12 (left: transfer trajectory; center: u, S, m; right: P_{in}, I_{sp}, $T_{\max}$).

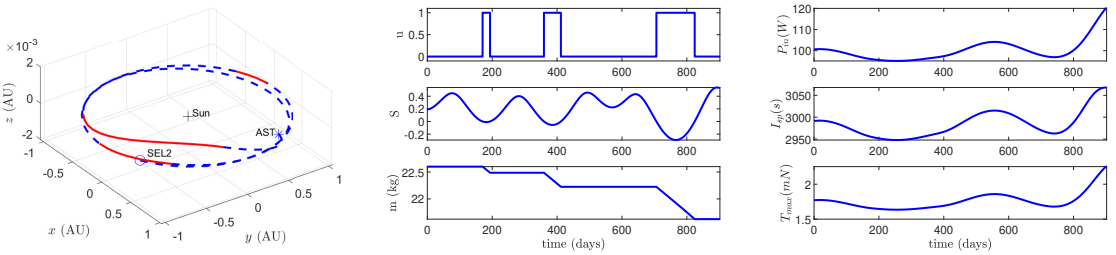

(c) Solution corresponding to point C in Fig. 12 (left: transfer trajectory; center: u, S, m; right: P_{in}, I_{sp}, $T_{\max}$).

Figure 13: Solutions corresponding to points A, B, C in Fig. 12 (departure epoch: 8600 MJD 2000). In trajectory plots, AST: asteroid location upon arrival; SEL2: Sun-Earth Lagrange L_2; red solid line: thrust segment; blue dashed line: coast segment.

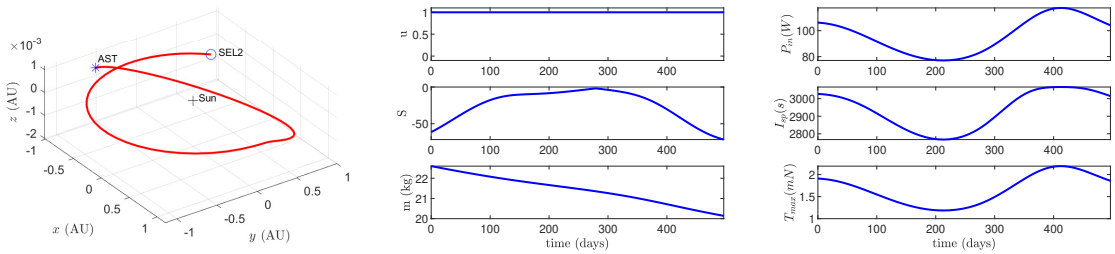

(a) Solution corresponding to point D in Fig. 12 (left: transfer trajectory; center: u, S, m; right: P_{in}, I_{sp}, $T_{\max}$).

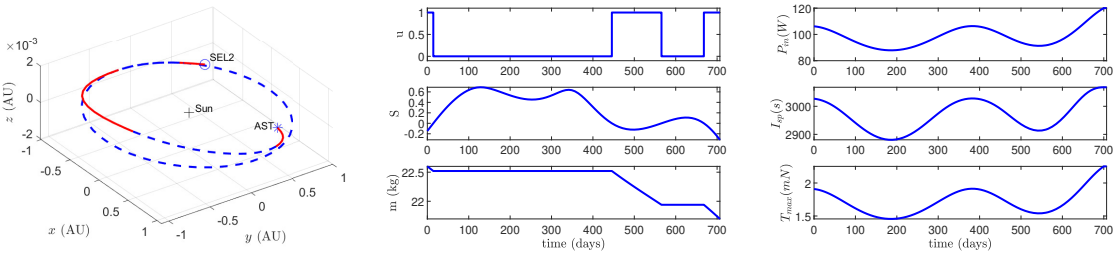

(b) Solution corresponding to point E in Fig. 12 (left: transfer trajectory; center: u, S, m; right: P_{in}, I_{sp}, $T_{\max}$).

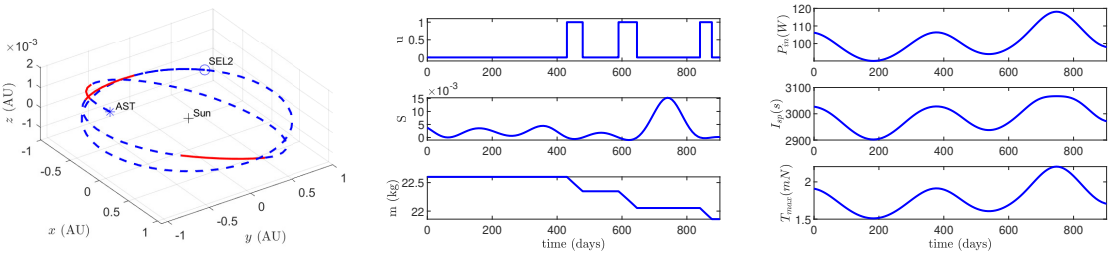

(c) Solution corresponding to point F in Fig. 12 (left: transfer trajectory; center: u, S, m; right: P_{in}, I_{sp}, $T_{\max}$).

Figure 14: Solutions corresponding to points D, E, F in Fig. 12 (departure epoch: 8800 MJD 2000). In trajectory plots, AST: asteroid location upon arrival; SEL2: Sun-Earth Lagrange L_2; red solid line: thrust segment; blue dashed line: coast segment.

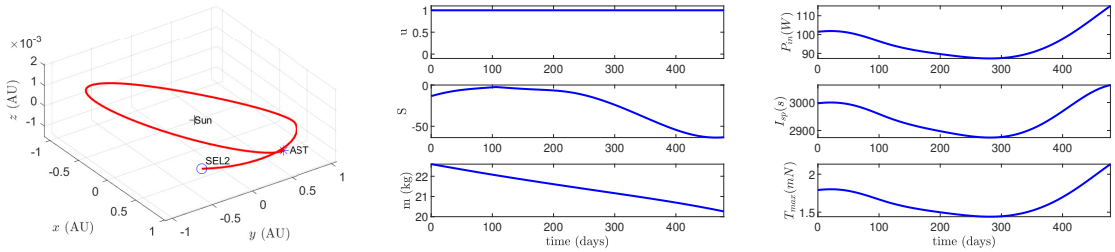

(a) Solution corresponding to point G in Fig. 12 (left: transfer trajectory; center: u, S, m; right: P_{in}, I_{sp}, $T_{\max}$).

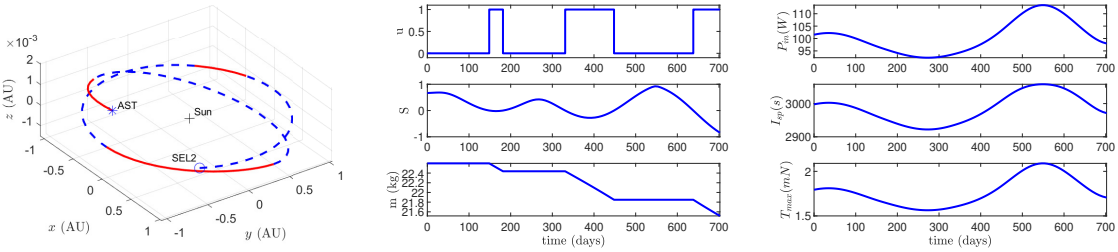

(b) Solution corresponding to point H in Fig. 12 (left: transfer trajectory; center: u, S, m; right: P_{in}, I_{sp}, $T_{\max}$).

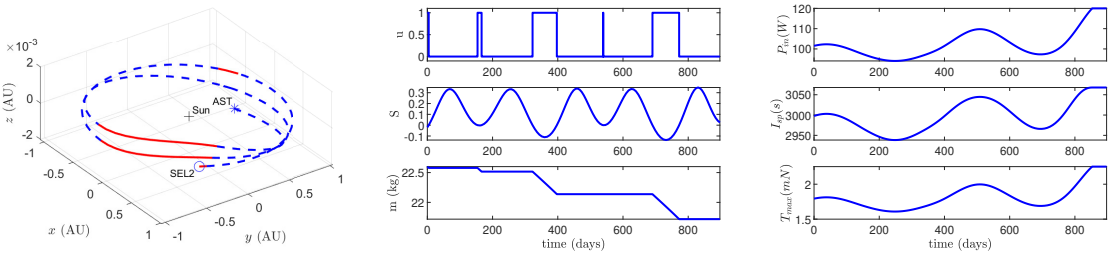

(c) Solution corresponding to point I in Fig. 12 (left: transfer trajectory; center: u, S, m; right: P_{in}, I_{sp}, $T_{\max}$).

Figure 15: Solutions corresponding to points G, H, I in Fig. 12 (departure epoch: 9000 MJD 2000). In trajectory plots, AST: asteroid location upon arrival; SEL2: Sun-Earth Lagrange L_2; red solid line: thrust segment; blue dashed line: coast segment.

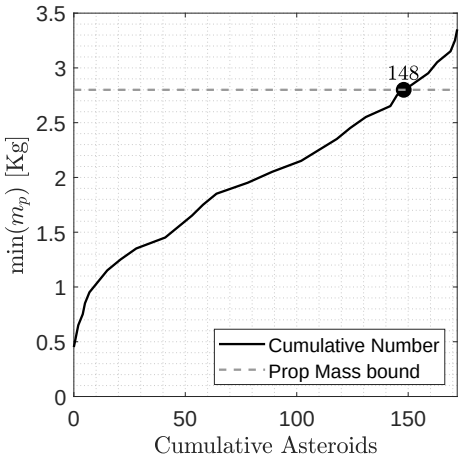

Figure 16: Cumulative number of asteroids for increasing global minimum propellant mass. The available propellant mass ($m_{p,\max} = 2.8$ kg) is indicated by the dashed line, while the number shows the number of asteroids below the threshold.

Table 7: NEO target screening process and results.

Step	**Target screening step**	**No. of objects**
#1	Asteroids in the Minor Planet Center database	900,000+
#2	Potential targets after orbital parameters pre-filtering	456
#3	Possible targets after minimum-time optimisation and pruning	172
#4	Reachable targets after minimum-fuel optimisation and pruning	148
#5	Downselected targets after statistical, pork chop analysis	41

A. Although the transfer time of the reachable targets is below the 3-year threshold, short-lasting solutions are preferred over relatively longer ones (this involves, e.g., less mission operation costs, less spacecraft cumulated radiation, etc.);

B. Although the propellant mass of the reachable targets is below the 2.8-kg threshold, low-propellant solutions are preferred over those requiring relatively higher values (this involves, e.g., having more room for avionics, launching a lighter CubeSat, etc.);

C. Although the reachable targets have at least one feasible solution within the 2-year departure window, those spanning the entire window are preferred over those that partially cover it, the departure epoch not being fixed (this assures mission robustness

against uncertainties in the departure time).

By enforcing criteria A, B, and C above, a high number of targets can be excluded from the subsequent analysis. In particular, with reference to Appendix C: 40 asteroids have a relatively long transfer time (condition A, see Table 8); 31 asteroids have a relatively high propellant mass (condition B, see Table 9); 36 asteroids do not span the full departure window (condition C, see Table 10). Thus, a total number of 107 asteroids is excluded from the solution space. It is worth mentioning that sometimes two or even three of the conditions above apply simultaneously.

Table 8: List of targets requiring long transfer time (40).

2007 WU3	2008 GM2	2011 MQ3	2012 WH	2016 FZ13	2016 RN20
2016 YR	2017 BZ6	2017 HK1	2017 JB2	2017 KJ32	2017 QB35
2017 RL16	2018 FM2	2018 LE1	2018 LQ2	2018 NX	2019 AU
2019 AC3	2019 DH1	2019 KM2	2019 LB1	2009 CV	YORP
2004 QA22	2007 VU6	2010 FY9	2011 OJ45	2013 VM13	2014 HN2
2014 MZ17	2014 UN114	2014 WU200	2015 JD3	2015 TC25	2016 TY55
2017 QW1	2018 FH1	2018 PR7	2018 WV1		

Table 9: List of targets requiring high propellant mass (31).

2014 EK24	1999 CG9	2005 QP11	2007 BB	2007 RO17	2010 WU8
2011 AA37	2012 AQ	2012 HK31	2012 PB20	2012 SX49	2012 VC26
2013 TG6	2014 FW32	2014 HW	2015 XD169	2015 XC352	2015 YK
2016 CH30	2016 EU84	2016 HF19	2018 FM3	2018 PN22	2018 SD2
2018 UE1	2019 GE1	2016 SX1	2017 UQ6	2017 YD1	2017 YS1
2017 VT7					

After filtering the list of reachable asteroids by virtue of criteria A, B, and C, the 41 targets listed in Table 11 are found. Since the mission and spacecraft design had to be tailored over five reference cases, (as per the statement of work, see Acknowledgments Section), a choice has been made considering the following properties:

- Information in LCDB: this is a desirable information to have as it is associated to more knowledge of the target;

Table 10: List of targets not spanning the full departure window (36).

1991 VG	1999 AO10	2000 SZ162	2001 GP2	2004 VJ1	2006 JY26
2006 RH120	2007 UN12	2008 EA9	2008 KT	2009 HC	2010 HA
2011 CE22	2011 CL50	2011 ED12	2012 FM35	2013 GH66	2013 RZ53
2014 BA3	2015 DU	2017 TP4	2018 GR4	2018 KP1	2018 PK21
2018 PM28	2018 TS4	2018 VN5	2019 ED	2019 GV5	2008 UA202
2010 TE55	2013 BS45	2014 QN266	2014 YP44	2015 PS228	2016 GK135

Table 11: List of downselected targets (41).

2012 UV136	2000 SG344	2001 QJ142	2008 CM74	2008 DL4	2008 HU4
2008 JL24	2008 ST	2009 BD	2010 JR34	2010 UE51	2011 BQ50
2011 MD	2011 WU2	2012 BB14	2012 EP10	2012 TF79	2014 JR24
2014 LJ	2014 YD	2014 YN	2015 BM510	2015 KK57	2015 VU64
2015 VO142	2015 XZ378	2016 BQ	2016 CF137	2016 DF	2016 FU12
2016 TB18	2016 TB57	2016 WQ3	2017 DV35	2017 RL2	2017 YW3
2018 DC4	2018 GE	2019 AP8	2019 DJ1	2019 GF1	

- Information known on spin-rate: like the light curve, this is desirable to have;
- Observability in future: the possibility to observe the target in the future allows refining the orbital uncertainty, so increasing the chances of in-orbit detection;
- Promising targets: the targets being less sensitive to the departure epoch and transfer time have been favoured over others.

The five temporary targets suggested for the mission and spacecraft design are:

1. **2014 YD**: Known high spin rate close to barrier and favourable mission opportunity;
2. **2010 UE51**: #1 on time-optimal and fuel-optimal solution list;
3. **2011 MD**: Present in light curve database and favourable mission opportunity.
4. **2000 SG344**: Chance for observation, higher inclination, good OCC [9];

[9]OCC is the Orbit Condition Code, where 0 implies a well-determined orbit and 9 implies a poorly determined orbit (Desmars et al., 2011).

5. **2012 UV136**: Known spin rate, largest target size/brightest.

The orbital parameters of these five sample targets are reported in Table 12.

Table 12: Orbital elements for the selected 5 asteroids (ecliptic J2000).

Name	a [AU]	e [-]	i [deg]	ω [deg]	Ω [deg]
2000 SG344	0.9775	0.0669	0.1121	275.3026	191.9599
2010 UE51	1.0552	0.0597	0.6239	47.2479	32.2993
2011 MD	1.0562	0.0371	2.4455	5.9818	271.5986
2012 UV136	1.0073	0.1392	2.2134	288.6071	209.9001
2014 YD	1.0721	0.0866	1.7357	34.1161	117.6401

8. Conclusions

This paper elaborates on the NEA targets screening for the M-ARGO mission. A multi-step filtering activity has been performed to identify a subset of asteroids reachable by the M-ARGO CubeSat. Bounds on orbital elements have reduced the Minor Planet Center database list of asteroids to 456 objects. Out of these, 172 objects require less than 900 days and 4 kg for the time-optimal solution. Then, 148 asteroids require less than 2.8 kg for the fuel-optimal solution. The list of 148 shapes the envelop of reachable targets by the M-ARGO CubeSat. Considering desirable mission parameters, the list is further reduced to 41 downselected objects, out of which 5 samples are extracted.
The outcome of this work is valid for M-ARGO mission under current assumptions of departure dates and thruster model. As for the latter, it is worth observing that $P_{\min}$ is never reached by optimal solutions. Should this be the case in future iterations, the rankings would be affected. The same applies to $P_{\max}$ as well as to the other thruster coefficients in Table 3.

9. Acknowledgments

The work described in this paper has been conducted within the study "Miniaturised Asteroid Remote Geophysical Observer (M-ARGO) IOD CubeSat Mission Phase A Study", ESA contract No. 4000127373/19/NL/AF. The authors would like to acknowledge the Minor Planet Center (MPC) at the Smithsonian Astrophysical Observatory (SAO) for maintaining the minor planet database.

10. Conflict of Interest Statement

The authors have participated in the M-ARGO Phase A mission study (see Acknowledgments Section).

References

Acton, C., Bachman, N., Semenov, B., and Wright, E. (2018). A look towards the future in the handling of space science mission geometry. *Planetary and Space Science*, 150:9–12. DOI: 10.1016/j.pss.2017.02.013.

Bowell, E., Hapke, B., Domingue, D., et al. (1989). Application of photometric models to asteroids. *Asteroids II*, pages 524–556.

Bryson, A. E. and Ho, Y.-C. (1975). *Applied Optimal Control: Optimization, Estimation and Control*. Taylor and Francis Group.

Cipriano, A., Dei Tos, D., and Topputo, F. (2018). Orbit design for LUMIO: The Lunar Meteoroid Impacts Observer. *Frontiers in Astronomy and Space Sciences*, 5:29. DOI: 10.3389/fspas.2018.00029.

Dei Tos, D. A. and Baresi, N. (2020). Genetic optimization for the orbit maintenance of libration point orbits with applications to EQUULEUS and LUMIO. In *AIAA Scitech 2020 Forum*, pages 1–18. DOI: 10.2514/6.2020-0466.

Desmars, J., Bancelin, D., Hestroffer, D., and Thuillot, W. (2011). Statistical analysis on the uncertainty of asteroid ephemerides. In *SF2A 2011: Annual meeting of the French Society of Astronomy and Astrophysics*, pages pp–639.

Ferrari, F., Franzese, V., Pugliatti, M., Giordano, C., and Topputo, F. (2021). Preliminary mission profile of Hera's Milani CubeSat. *Advances in Space Research*. DOI: 10.1016/j.asr.2020.12.034.

Franzese, V., Di Lizia, P., and Topputo, F. (2019). Autonomous optical navigation for the lunar meteoroid impacts observer. *Journal of Guidance, Control, and Dynamics*, 42(7):1579–1586. DOI: 10.2514/1.G003999.

Giorgini, J. and Yeomans, D. (1999). On-line system provides accurate ephemeris and related data. *NASA TECH BRIEFS, NPO-20416*, 48.

Goldberg, H., Karatekin, Ö., Ritter, B., Herique, A., et al. (2019). The Juventas CubeSat in support of ESA's Hera mission to the asteroid Didymos. In *Small Satellite Conference, Logan, Utah*, pages 1–7.

Harris, A. W. (1997). On the revision of radiometric albedos and diameters of asteroids. *Icarus*, 126(2):450–454. DOI: 10.1006/icar.1996.5664.

Klesh, A. and Krajewski, J. (Logan, UT, 2015). MarCO: CubeSats to Mars in 2016. In *29th Annual AIAA/USU Conference on Small Satellites*, pages 1–7.

Kruzelecky, R. (2018). VMMO Lunar Volatile and Mineralogy Mapping 12U Cubesat. *42nd COSPAR Scientific Assembly.* 14-22 July 2018, Pasadena, California, USA.

Lockett, T. R., Castillo-Rogez, J., Johnson, L., Matus, J., et al. (2020). Near-Earth Asteroid Scout flight mission. *IEEE Aerospace and Electronic Systems Magazine*, 35(3):20–29. DOI: 10.1109/MAES.2019.2958729.

Machuca, P., Sanchez, J. P., Masdemont, J. J., and Gomez, G. (2020). High-fidelity trajectory design to flyby near-Earth asteroids using CubeSats. *Acta Astronautica*, 167:146–163. DOI: 10.1016/j.actaastro.2019.09.041.

Malphrus, B. K., Freeman, A., Staehle, R., et al. (2020). *Interplanetary CubeSat missions.* Elsevier.

McIntosh, D. M., Baker, J. D., and Matus, J. A. (2020). The NASA CubeSat missions flying on Artemis-1. In *Small Satellite Conference*, pages 1–11. Utah State University, Logan, UT.

Mereta, A. and Izzo, D. (2018). Target selection for a small low-thrust mission to near-Earth asteroids. *Astrodynamics*, 2(3):249–263. DOI: 10.1007/s42064-018-0024-y.

Michel, P., Küppers, M., and Carnelli, I. (Pasadena, California, 2018). The Hera mission: European component of the ESA–NASA AIDA mission to a binary asteroid. In *42nd COSPAR Scientific Assembly*, volume 42 of *COSPAR Meeting*, pages 1–42.

Oguri, K., Oshima, K., Campagnola, S., Kakihara, K., et al. (2020). EQUULEUS trajectory design. *The Journal of the Astronautical Sciences*, pages 1–27. DOI: 10.1007/s40295-019-00206-y.

Peloni, A., Ceriotti, M., and Dachwald, B. (2016). Solar-sail trajectory design for a multiple near-Earth-asteroid rendezvous mission. *Journal of Guidance, Control, and Dynamics*, 39(12):2712–2724. DOI: 10.2514/1.G000470.

Poghosyan, A. and Golkar, A. (2017). CubeSat evolution: Analyzing CubeSat capabilities for conducting science missions. *Progress in Aerospace Sciences*, 88:59–83. DOI: 10.1016/j.paerosci.2016.11.002.

Qiao, D., Cui, H., and Cui, P. (2006). Evaluating accessibility of near-Earth asteroids via Earth gravity assists. *Journal of Guidance, Control, and Dynamics*, 29(2):502–505. DOI: 10.2514/1.16757.

Russell, R. P. (2007). Primer vector theory applied to global low-thrust trade studies. *Journal of Guidance, Control, and Dynamics*, 30(2):460–472. DOI: 10.2514/1.22984.

Schoolcraft, J., Klesh, A., and Werne, T. (2017). MarCO: interplanetary mission development on a CubeSat scale. In *Space Operations: Contributions from the Global Community*, pages 221–231. Springer. DOI: 10.1007/978-3-319-51941-8_10.

Speretta, S., Cervone, A., Sundaramoorthy, P., et al. (2019). *LUMIO: An autonomous CubeSat for Lunar exploration*, chapter 6, pages 103–134. Springer International Publishing. DOI: 10.1007/978-3-030-11536-4_6.

Topputo, F., Dei Tos, D. A., Mani, K., et al. (2018a). Trajectory design in high-fidelity models. In *7th International Conference on Astrodynamics Tools and Techniques (ICATT), 6-9 November 2018, Oberpfaffenhofen, Germany*, pages 1–9.

Topputo, F., Massari, M., Biggs, J., et al. (Sorrento, 2018b). LUMIO: A CubeSat at Earth-Moon L2. In *4S Symposium*, pages 1–15.

Vallado, D. A. (2013). *Fundamentals of astrodynamics and applications.* Microcosm Press and Springer, Hawthorne, CA, 4th edition.

Wagner, S., Wie, B., and Barbee, B. W. (2015). Target selection for a hypervelocity asteroid intercept vehicle flight validation mission. *Acta Astronautica*, 107:247–261. DOI: 10.1016/j.actaastro.2014.11.037.

Walker, R., Binns, D., Bramanti, C., et al. (2018). Deep-space CubeSats: Thinking inside the box. *Astronomy & Geophysics*, 59(5):5–24. DOI: 10.1093/astrogeo/aty232.

Walker, R., Koschny, D., Bramanti, C., Carnelli, I., et al. (2017). Miniaturised asteroid remote geophysical observer (M-ARGO): a stand-alone deep space cubesat system for low-cost science and exploration missions. *iCubeSat Workshop, Cambridge*, pages 1–20.

Warner, B. D., Harris, A. W., and Pravec, P. (2009). The asteroid lightcurve database. *Icarus*, 202(1):134–146. DOI: 10.1016/j.icarus.2009.02.003.

Zhang, C., Topputo, F., Bernelli-Zazzera, F., and Zhao, Y. (2015). Low-thrust minimum-fuel optimization in the circular restricted three-body problem. *Journal of Guidance, Control, and Dynamics*, 38(8):1501–1510. DOI: 10.2514/1.G001080.

Appendix A. Rankings of time-optimal transfers

Time-optimal transfers are ranked here below. #: position in the ranking; Name: asteroid name; $\tau_{\min}$: minimum transfer time; $m_p(\tau_{\min})$: fuel consumption corresponding to the minimum-time solution; Dep. Date: departure date; H: absolute magnitude; D: estimated diameter; N_{obs}: number of observations; N_{opp}: number of oppositions.

#	Name	$\tau_{\min}$ [d]	$m_p(\tau_{\min})$ [kg]	Dep. Date	H [-]	D [m]	N_{obs}	N_{opp}
1	2010 UE51	131.82	0.693	04 Mar 2023	28.3	7.5	175	1
2	2015 KK57	295.28	1.359	03 Oct 2023	27.5	10.9	43	1
3	2011 MD	302.11	1.597	07 Jan 2023	28	8.6	1487	1
4	2009 BD	312.82	1.441	01 Jan 2023	28.1	8.2	178	3
5	2016 TB57	340.70	1.611	05 Dec 2024	26.1	20.7	137	1
6	2014 JR24	345.15	1.966	01 Jan 2023	29.3	4.7	54	1
7	2019 DJ1	349.56	1.770	31 Dec 2024	26.7	15.7	82	2
8	2016 CF137	352.89	1.656	05 Dec 2024	25.6	26.0	50	1
9	2014 BA3	355.69	2.032	17 Nov 2023	28.2	7.9	69	1
10	2012 BB14	361.40	1.793	04 Apr 2023	25	34.3	35	2
11	2014 LJ	367.31	1.699	21 May 2024	28.5	6.8	25	1
12	2017 YW3	370.33	1.968	31 Dec 2024	26.5	17.2	53	1
13	2008 CM74	373.96	2.028	24 Apr 2024	28.1	8.2	17	1
14	2012 EP10	378.58	2.066	16 Dec 2024	29.1	5.2	31	1
15	2008 ST	384.77	2.098	19 Jun 2023	27.1	13.0	49	1
16	2014 YD	395.10	1.932	31 Dec 2024	24.3	47.4	104	1
17	2017 RL2	402.66	1.860	22 Jul 2023	26.1	20.7	44	1
18	2001 QJ142	410.17	2.005	15 May 2023	23.7	62.4	91	2
19	2011 BQ50	419.76	2.488	01 Jan 2023	28	8.6	25	1
20	2010 JR34	421.98	2.464	31 Dec 2024	27.7	9.9	36	1
21	2012 UV136	423.38	2.088	06 Feb 2023	25.5	27.3	125	7

22	2000 SG344	427.48	2.109	10 Jun 2024	24.7	39.4	31	2
23	2015 VO142	427.82	2.339	15 Nov 2024	28.9	5.7	112	1
24	2008 JL24	432.43	2.390	01 Jan 2023	29.6	4.1	81	1
25	2015 VU64	435.24	2.507	01 Jan 2023	30.6	2.6	30	1
26	2018 GE	441.42	2.430	31 Dec 2024	27.5	10.9	54	1
27	2016 EU84	446.65	2.576	31 Dec 2024	29	5.4	94	1
28	2015 XD169	446.86	2.330	18 Jul 2023	26.9	14.3	46	1
29	2016 WQ3	452.13	2.077	31 Dec 2024	28.8	6.0	37	1
30	2019 ED	459.03	2.723	31 Dec 2024	26.9	14.3	67	1
31	2017 KJ32	459.49	2.670	12 Mar 2023	28.9	5.7	37	1
32	2017 HK1	459.85	2.646	13 Apr 2023	25.1	32.8	78	1
33	2019 AP8	461.14	1.989	31 Dec 2024	24.3	47.4	68	2
34	2019 GF1	472.58	2.810	22 Aug 2024	27.4	11.4	27	1
35	2008 DL4	479.15	2.790	31 Dec 2024	26.9	14.3	29	1
36	2017 DV35	479.49	2.755	24 Oct 2024	27.2	12.5	43	1
37	2011 WU2	479.65	2.152	19 Jun 2023	24.9	35.9	14	1
38	2014 YN	485.35	2.799	19 Nov 2023	25.7	24.9	80	1
39	2009 HC	487.47	2.757	15 Jun 2024	24.7	39.4	145	1
40	2018 TS4	493.54	2.671	20 Jul 2023	27.6	10.4	28	1
41	1999 AO10	497.74	2.773	31 Dec 2024	23.9	56.9	73	1
42	2016 TB18	502.17	2.822	18 Jun 2023	24.8	37.6	96	1
43	2015 BM510	503.39	2.676	03 Aug 2024	25.1	32.8	58	1
44	2013 TG6	504.07	2.882	17 Oct 2024	26.6	16.4	63	1
45	2012 SX49	510.97	2.885	31 Dec 2024	26.2	19.7	35	1
46	2018 PK21	511.00	3.025	12 Oct 2023	25.9	22.7	72	1
47	2016 BQ	511.59	2.598	30 Apr 2023	26.8	15.0	40	1
48	2016 FU12	514.43	2.631	24 Oct 2023	26.9	14.3	19	1
49	2016 HF19	515.16	2.960	11 Nov 2024	26.5	17.2	90	1
50	2018 PN22	516.02	2.932	01 Jan 2023	27.5	10.9	17	1
51	2018 DC4	516.59	3.016	18 May 2023	27.3	11.9	19	1
52	2011 ED12	520.33	2.824	31 Dec 2024	26.8	15.0	82	1
53	2016 CH30	521.75	2.872	01 Jan 2023	28	8.6	34	1
54	2011 CL50	526.32	3.016	03 Jun 2023	27.6	10.4	28	1
55	2012 VC26	531.30	2.897	09 Jul 2024	28.7	6.2	28	1
56	2012 TF79	531.37	2.998	04 Jun 2024	27.4	11.4	59	1
57	2008 HU4	532.62	2.979	31 Dec 2024	28.3	7.5	77	2
58	2015 XZ378	536.69	2.486	14 Apr 2024	27.2	12.5	35	1
59	2016 DF	542.00	2.623	15 Jun 2024	27	13.7	45	1
60	2010 HA	545.07	2.865	20 Sep 2023	23.9	56.9	62	2
61	2018 VN5	549.44	2.892	31 Dec 2024	25.4	28.5	94	1
62	2007 BB	550.99	2.986	01 Jan 2023	27.8	9.5	20	1
63	2019 GE1	552.81	2.896	26 Jun 2023	27	13.7	17	1

64	2000 SZ162	568.64	3.119	15 Aug 2023	27.3	11.9	30	1
65	2014 FW32	569.12	3.311	31 Dec 2024	27	13.7	23	1
66	2014 HW	569.71	2.852	03 Mar 2023	28.4	7.2	28	1
67	2018 NX	572.39	3.200	26 Apr 2024	27.7	9.9	28	1
68	2001 GP2	574.12	2.613	14 Jul 2023	26.9	14.3	28	1
69	2018 KP1	576.44	2.782	01 Jan 2023	25.1	32.8	50	2
70	2011 CE22	581.04	2.837	19 Jun 2023	25.4	28.5	18	1
71	2007 RO17	582.26	3.148	13 Jan 2023	25.8	23.7	18	1
72	2010 TE55	583.87	3.557	06 Oct 2024	28	8.6	139	1
73	2006 RH120	589.52	3.376	12 Mar 2023	29.5	4.3	133	2
74	2019 GV5	590.94	3.116	15 Mar 2023	29.3	4.7	31	1
75	2013 GH66	591.70	3.417	31 Dec 2024	28	8.6	46	1
76	2014 EK24	592.30	2.950	24 Oct 2024	23.3	75.1	583	2
77	2012 WH	593.13	3.319	27 May 2024	25.5	27.3	43	1
78	2004 VJ1	594.69	3.010	07 Jan 2023	24.1	51.9	98	2
79	2017 QB35	595.29	3.314	31 Dec 2024	29.3	4.7	33	1
80	2014 YP44	597.54	3.665	17 Sep 2024	26.1	20.7	13	1
81	2013 BS45	604.69	3.710	30 Aug 2023	25.9	22.7	92	2
82	2010 WU8	605.66	3.103	14 Jul 2024	24.2	49.6	24	1
83	2018 PM28	605.99	2.742	01 Jan 2023	25.7	24.9	46	2
84	2018 LQ2	606.60	3.363	31 Dec 2024	24.9	35.9	468	1
85	2016 GK135	607.52	3.679	17 Jul 2023	28.1	8.2	21	1
86	2018 SD2	611.04	3.161	16 Oct 2024	28.6	6.5	14	1
87	2019 LB1	614.23	3.471	01 Jan 2023	27	13.7	61	1
88	2017 TP4	615.43	3.403	18 Sep 2024	26.3	18.9	41	1
89	2008 UA202	616.60	3.687	31 Dec 2024	29.4	4.5	16	1
90	2018 FM3	617.95	2.961	22 Oct 2023	27.2	12.5	47	1
91	2014 QN266	618.60	3.707	14 Mar 2023	26.3	18.9	81	1
92	2011 AA37	619.08	3.373	01 Jan 2023	22.8	94.5	130	2
93	2018 VT7	619.15	3.784	04 Dec 2023	27.9	9.0	23	1
94	2013 RZ53	619.45	2.775	24 Apr 2023	31.1	2.1	31	1
95	2017 QW1	619.56	3.741	17 Aug 2023	26.2	19.7	36	1
96	2016 CO248	620.02	3.592	10 Dec 2023	27.5	10.9	30	1
97	2016 SX1	620.71	3.584	08 Dec 2024	28.6	6.5	37	1
98	2015 YK	623.23	2.960	16 Dec 2023	25.9	22.7	96	1
99	2014 HN2	625.70	3.810	02 Jan 2023	26.5	17.2	64	1
100	2015 JD3	629.20	3.583	01 Jan 2023	25.5	27.3	37	1
101	2017 UA45	632.36	3.526	14 Nov 2023	26.1	20.7	39	1
102	2019 AU	634.09	3.168	12 Nov 2024	26.7	15.7	48	1
103	2015 PS228	639.44	3.830	24 Mar 2023	28.8	6.0	38	1
104	2019 HM	640.18	3.761	25 Feb 2023	25.9	22.7	32	1
105	2017 YS1	644.07	3.913	01 Jan 2023	28.9	5.7	31	1

106	2018 GR4	644.78	3.150	31 Dec 2024	27.1	13.0	64	1
107	2016 RN20	645.02	3.463	31 Dec 2024	28.2	7.9	19	1
108	2012 PB20	646.80	3.431	31 Dec 2024	24.9	35.9	45	1
109	2010 FY9	647.95	3.522	31 Dec 2024	26.7	15.7	22	1
110	2012 AQ	653.45	2.821	01 Jan 2023	30.7	2.5	24	1
111	2017 YD1	654.94	3.665	16 Jan 2024	30	3.4	29	1
112	2019 FS2	657.28	3.952	01 Jan 2023	27.3	11.9	46	1
113	1999 CG9	662.48	3.058	11 Jan 2023	25.2	31.3	42	1
114	2018 RO5	662.50	3.592	16 Jun 2024	25.6	26.0	96	1
115	2017 BZ6	662.73	3.469	13 Sep 2024	26.1	20.7	71	1
116	2012 HK31	666.02	2.988	01 Nov 2023	25.4	28.5	63	1
117	2010 XF3	666.52	3.990	16 Feb 2024	24.4	45.2	94	1
118	2014 UN114	666.60	3.520	01 Jan 2023	24.5	43.2	177	1
119	2016 FZ13	668.88	3.346	19 Feb 2023	28.3	7.5	20	1
120	2015 XC352	670.87	3.177	26 Jan 2023	25.7	24.9	75	2
121	2015 DU	671.74	2.859	15 Sep 2023	26.6	16.4	96	1
122	2016 HF2	675.09	3.860	23 Jul 2023	26.1	20.7	77	1
123	2018 ER1	680.94	3.541	31 Dec 2024	25.6	26.0	61	1
124	2016 LC9	685.49	3.803	05 Jul 2024	27	13.7	30	1
125	2019 JN2	689.59	3.396	07 Apr 2023	25.7	24.9	47	1
126	2006 JY26	690.41	3.111	31 Dec 2024	28.4	7.2	76	1
127	2005 QP11	698.41	3.345	31 Dec 2024	26.4	18.0	53	1
128	2012 FM35	698.42	3.108	25 Jul 2024	27.3	11.9	77	1
129	2019 GM1	699.46	3.804	31 Dec 2024	27.5	10.9	14	1
130	2008 KT	699.94	3.140	22 Jul 2023	28.2	7.9	30	1
131	2007 UN12	704.27	3.080	31 Dec 2024	28.7	6.2	120	1
132	2017 RL16	707.17	3.241	29 Jul 2024	25	34.3	51	1
133	2018 SF3	708.99	3.605	08 Aug 2023	25.2	31.3	31	1
134	2019 AC3	712.91	3.230	31 Oct 2024	27.3	11.9	43	1
135	2013 UT4	714.24	3.335	27 Jun 2024	26.2	19.7	24	1
136	2018 UE1	723.22	3.416	01 Jan 2023	26.7	15.7	55	1
137	2017 DR109	724.49	3.414	31 Dec 2024	27.6	10.4	28	1
138	2017 UQ6	726.82	3.532	25 Sep 2024	27.2	12.5	25	1
139	2017 KU34	729.10	3.418	02 Sep 2023	23.6	65.4	78	3
140	2014 AE29	729.65	3.824	15 Jan 2023	27.4	11.4	26	1
141	2011 MQ3	736.52	3.326	31 Dec 2024	24.8	37.6	71	1
142	2013 VM13	739.72	3.572	09 Mar 2023	23.9	56.9	46	2
143	2008 EA9	744.24	3.118	04 Apr 2023	27.7	9.9	56	1
144	2014 MZ17	745.60	3.549	05 Jan 2023	24.1	51.9	47	2
145	2018 FM2	746.00	3.497	08 Apr 2023	26.6	16.4	18	1
146	2017 FP101	747.34	3.972	01 Jan 2023	24.7	39.4	48	1
147	2008 GM2	747.74	3.254	20 Jul 2024	28.3	7.5	54	1

148	2016 YR	748.47	3.279	31 Dec 2024	27.2	12.5	52	1
149	2017 JB2	749.62	3.418	24 Jan 2023	29.2	5.0	33	1
150	2007 WU3	750.25	3.382	23 Dec 2024	23.8	59.6	35	3
151	2016 EE28	752.08	3.391	25 Feb 2023	26.8	15.0	22	1
152	1991 VG	755.50	3.193	18 Nov 2024	28.3	7.5	66	3
153	2009 CV	763.83	3.240	02 Jul 2023	24.3	47.4	174	4
154	2013 WR45	776.78	3.620	01 Jan 2023	25.7	24.9	22	1
155	2019 KM2	788.09	3.420	27 Jul 2023	25.5	27.3	14	1
156	2018 FH1	794.30	3.866	20 Dec 2024	26.6	16.4	43	1
157	2019 DH1	796.84	3.423	14 Mar 2023	26.2	19.7	53	1
158	2018 LE1	799.03	3.489	13 Apr 2024	27.5	10.9	55	1
159	2018 PR7	804.18	3.534	27 Apr 2023	28.5	6.8	55	1
160	2014 JX54	810.60	3.425	16 Jun 2023	24.4	45.2	17	1
161	2011 OJ45	811.69	3.551	17 Oct 2023	26	21.6	21	1
162	YORP	818.52	3.687	30 Sep 2023	22.7	99.0	533	5
163	2009 BK2	830.55	3.780	15 Aug 2024	25.3	29.9	27	1
164	2001 GO2	842.00	3.780	13 Jul 2023	24.3	47.4	23	1
165	2018 WV1	843.23	3.636	22 Jul 2024	30.3	3.0	87	1
166	2004 QA22	844.14	3.845	25 Sep 2024	27.9	9.0	44	1
167	2016 TY55	852.18	3.724	26 Jan 2023	26.9	14.3	44	1
168	2014 WU200	855.27	3.558	08 Sep 2023	29.1	5.2	46	1
169	2015 TC25	858.58	3.716	01 Jan 2023	29.3	4.7	44	2
170	2007 VU6	864.20	3.890	07 May 2023	26.5	17.2	38	1
171	2019 LE1	875.50	3.831	01 Jan 2023	26.4	18.0	28	1
172	2018 XX3	878.36	3.778	09 Jan 2023	29.7	3.9	23	1

Table A.13: Ranking of time-optimal transfers.

Appendix B. Ranking of fuel-optimal transfers

Fuel-optimal transfers are ranked here below. $m_{p,\min}$: minimum fuel consumption; TOF: time of flight corresponding to the minimum-fuel solution.

#	Name	$m_{p,\min}$ [kg]	TOF [d]	Dep. Date	H [-]	D [m]	N_{obs}	N_{opp}
1	2010 UE51	0.452	1095	07 Nov 2023	28.3	7.5	175	1
2	2009 BD	0.638	1095	05 Feb 2024	28.1	8.2	178	3
3	2000 SG344	0.717	972.93	01 Jan 2023	24.7	39.4	31	2
4	2001 GP2	0.740	967.70	09 Aug 2023	26.9	14.3	28	1
5	2015 KK57	0.848	720.62	01 Jan 2023	27.5	10.9	43	1
6	2016 TB57	0.873	920.64	05 Feb 2024	26.1	20.7	137	1
7	2008 JL24	0.917	1089.18	27 Nov 2023	29.6	4.1	81	1

8	2014 YD	0.969	1089.88	21 Apr 2023	24.3	47.4	104	1
9	2012 TF79	0.985	1072.06	14 Jun 2024	27.4	11.4	59	1
10	2008 HU4	1.033	1095	05 May 2024	28.3	7.5	77	2
11	2011 MD	1.035	1071.06	11 Dec 2024	28	8.6	1487	1
12	2016 TB18	1.052	1093.60	30 Jul 2023	24.8	37.6	96	1
13	2012 EP10	1.056	1059.41	21 Dec 2024	29.1	5.2	31	1
14	2016 WQ3	1.100	1038.50	21 May 2023	28.8	6.0	37	1
15	2015 VO142	1.122	1000.31	01 Apr 2023	28.9	5.7	112	1
16	2014 QN266	1.173	1079.37	09 Aug 2023	26.3	18.9	81	1
17	2018 TS4	1.192	1070.21	02 Mar 2023	27.6	10.4	28	1
18	2019 GF1	1.208	1095	15 May 2024	27.4	11.4	27	1
19	2006 RH120	1.221	1095	28 Oct 2023	29.5	4.3	133	2
20	2015 XZ378	1.240	1095	01 Jan 2023	27.2	12.5	35	1
21	2017 TP4	1.242	1095	11 Jan 2023	26.3	18.9	41	1
22	2008 UA202	1.261	1095	14 Jul 2024	29.4	4.5	16	1
23	2015 PS228	1.277	1080.73	06 Mar 2024	28.8	6.0	38	1
24	2006 JY26	1.307	1095	19 Aug 2023	28.4	7.2	76	1
25	2007 UN12	1.316	1095	16 Jan 2024	28.7	6.2	120	1
26	2017 RL2	1.323	1084.56	11 Apr 2023	26.1	20.7	44	1
27	2018 FM2	1.335	1072.13	26 Jan 2024	26.6	16.4	18	1
28	2018 GR4	1.339	933.23	07 Dec 2023	27.1	13.0	64	1
29	2016 CF137	1.352	912.60	08 Sep 2023	25.6	26.0	50	1
30	2018 PM28	1.358	1048.49	01 Jan 2023	25.7	24.9	46	2
31	2014 JR24	1.369	1095	21 May 2023	29.3	4.7	54	1
32	2013 RZ53	1.374	1095	21 Nov 2024	31.1	2.1	31	1
33	2008 EA9	1.375	1095	20 Jul 2023	27.7	9.9	56	1
34	2014 LJ	1.396	795.84	17 Nov 2023	28.5	6.8	25	1
35	2018 PK21	1.401	968.35	10 Jul 2023	25.9	22.7	72	1
36	2017 UQ6	1.401	1095	21 Dec 2024	27.2	12.5	25	1
37	2019 AP8	1.404	1095	10 Jul 2023	24.3	47.4	68	2
38	2015 BM510	1.415	1037.66	21 Apr 2023	25.1	32.8	58	1
39	2017 YW3	1.417	845.92	15 Feb 2024	26.5	17.2	53	1
40	2018 LQ2	1.442	1095	01 Jan 2023	24.9	35.9	468	1
41	2008 ST	1.451	903.82	01 May 2023	27.1	13.0	49	1
42	2011 BQ50	1.474	1017.07	11 Dec 2024	28	8.6	25	1
43	2018 KP1	1.478	1095	01 Jan 2023	25.1	32.8	50	2
44	2008 KT	1.487	1095	30 Jul 2023	28.2	7.9	30	1
45	2018 GE	1.505	939.72	15 May 2024	27.5	10.9	54	1
46	2010 JR34	1.521	1061.92	21 Apr 2023	27.7	9.9	36	1
47	2013 BS45	1.524	1068.37	21 Dec 2024	25.9	22.7	92	2
48	2012 FM35	1.561	1073.42	02 Mar 2023	27.3	11.9	77	1
49	2008 CM74	1.618	1023.81	31 May 2023	28.1	8.2	17	1

50	2018 VN5	1.638	1095	03 Aug 2024	25.4	28.5	94	1
51	2012 BB14	1.645	1051.41	01 Jan 2023	25	34.3	35	2
52	1991 VG	1.645	1055.50	20 Jun 2023	28.3	7.5	66	3
53	2000 SZ162	1.645	982.97	10 Jul 2023	27.3	11.9	30	1
54	2019 DJ1	1.671	834.90	01 Jan 2023	26.7	15.7	82	2
55	2014 BA3	1.683	1095	10 Jul 2023	28.2	7.9	69	1
56	2012 UV136	1.686	1080.14	30 Jul 2023	25.5	27.3	125	7
57	2016 FU12	1.706	1041.21	01 Apr 2023	26.9	14.3	19	1
58	2001 QJ142	1.721	1078.27	05 Apr 2024	23.7	62.4	91	2
59	2015 JD3	1.772	1095	20 Jun 2023	25.5	27.3	37	1
60	2011 ED12	1.783	1095	24 Jun 2024	26.8	15.0	82	1
61	2004 VJ1	1.789	1090.48	01 Jan 2023	24.1	51.9	98	2
62	2015 VU64	1.792	902.88	10 Jul 2023	30.6	2.6	30	1
63	2010 TE55	1.827	1026.83	10 Jul 2023	28	8.6	139	1
64	2011 AA37	1.834	1058.16	21 Dec 2024	22.8	94.5	130	2
65	2015 DU	1.855	1095	28 Sep 2023	26.6	16.4	96	1
66	2011 WU2	1.865	1034.97	26 Mar 2024	24.9	35.9	14	1
67	2014 YN	1.867	933.26	21 Apr 2023	25.7	24.9	80	1
68	2013 GH66	1.873	1051.13	20 Feb 2023	28	8.6	46	1
69	1999 AO10	1.884	1072.70	31 May 2023	23.9	56.9	73	1
70	2012 HK31	1.884	1095	21 May 2023	25.4	28.5	63	1
71	2016 HF19	1.901	1095	07 Nov 2023	26.5	17.2	90	1
72	2007 VU6	1.911	1093.00	12 Mar 2023	26.5	17.2	38	1
73	2019 ED	1.916	1095	01 Jan 2023	26.9	14.3	67	1
74	2014 WU200	1.921	1095	27 Nov 2023	29.1	5.2	46	1
75	2012 AQ	1.929	1088.45	01 Dec 2024	30.7	2.5	24	1
76	2017 DV35	1.931	977.24	01 Jan 2023	27.2	12.5	43	1
77	2018 DC4	1.935	977.05	11 Dec 2024	27.3	11.9	19	1
78	2017 YD1	1.937	1095	21 Dec 2024	30	3.4	29	1
79	2016 DF	1.964	1016.21	27 Nov 2023	27	13.7	45	1
80	2018 VT7	1.965	1095	25 Feb 2024	27.9	9.0	23	1
81	2009 CV	1.985	1095	11 Jan 2023	24.3	47.4	174	4
82	2016 BQ	1.989	1095	01 Dec 2024	26.8	15.0	40	1
83	2011 CL50	1.993	972.21	20 Jul 2023	27.6	10.4	28	1
84	2008 DL4	1.998	875.56	01 Jan 2023	26.9	14.3	29	1
85	2018 WV1	2.012	1083.23	12 Mar 2023	30.3	3.0	87	1
86	2015 XD169	2.022	1095	31 Jan 2023	26.9	14.3	46	1
87	2014 EK24	2.029	1095	06 Jan 2024	23.3	75.1	583	2
88	2016 YR	2.046	1095	30 Jul 2023	27.2	12.5	52	1
89	2018 SD2	2.050	1095	21 May 2023	28.6	6.5	14	1
90	2013 VM13	2.056	1077.70	21 Dec 2024	23.9	56.9	46	2
91	2018 FM3	2.057	1093.49	22 Oct 2024	27.2	12.5	47	1

92	2016 CH30	2.067	1062.13	10 Jul 2023	28	8.6	34	1
93	2010 HA	2.071	1095	03 Aug 2024	23.9	56.9	62	2
94	2019 DH1	2.075	1095	01 Jan 2023	26.2	19.7	53	1
95	2018 PN22	2.099	1095	21 Nov 2024	27.5	10.9	17	1
96	2009 HC	2.101	1089.68	21 Dec 2024	24.7	39.4	145	1
97	2017 HK1	2.112	1095	28 Sep 2023	25.1	32.8	78	1
98	2004 QA22	2.127	1095	20 Feb 2023	27.9	9.0	44	1
99	2011 OJ45	2.129	1095	02 Oct 2024	26	21.6	21	1
100	2017 KJ32	2.146	971.47	21 Jan 2023	28.9	5.7	37	1
101	2012 SX49	2.147	1095	31 May 2023	26.2	19.7	35	1
102	2016 GK135	2.150	1095	10 Jun 2023	28.1	8.2	21	1
103	2019 GV5	2.169	1067.54	01 Jan 2023	29.3	4.7	31	1
104	2016 EU84	2.169	926.65	16 Jan 2024	29	5.4	94	1
105	2014 FW32	2.182	1095	21 Nov 2024	27	13.7	23	1
106	2012 VC26	2.185	1095	19 Aug 2023	28.7	6.2	28	1
107	2014 YP44	2.189	1095	02 Oct 2024	26.1	20.7	13	1
108	1999 CG9	2.198	1095	01 Dec 2024	25.2	31.3	42	1
109	2011 CE22	2.201	1095	11 Apr 2023	25.4	28.5	18	1
110	2019 AU	2.210	1095	20 Jun 2023	26.7	15.7	48	1
111	2014 HN2	2.269	1016.28	31 May 2023	26.5	17.2	64	1
112	2007 WU3	2.277	1095	10 Jun 2023	23.8	59.6	35	3
113	2016 SX1	2.279	1095	11 Jan 2023	28.6	6.5	37	1
114	2015 YK	2.295	948.47	10 Jul 2023	25.9	22.7	96	1
115	2017 RL16	2.318	1095	08 Sep 2023	25	34.3	51	1
116	2013 TG6	2.321	1007.76	13 Aug 2024	26.6	16.4	63	1
117	2019 KM2	2.331	1095	01 Jan 2023	25.5	27.3	14	1
118	2019 AC3	2.341	1095	02 Mar 2023	27.3	11.9	43	1
119	2016 RN20	2.352	1095	02 Mar 2023	28.2	7.9	19	1
120	2007 BB	2.395	1065.55	01 Apr 2023	27.8	9.5	20	1
121	2017 JB2	2.410	1095	25 Apr 2024	29.2	5.0	33	1
122	2010 WU8	2.412	1044.28	14 Jun 2024	24.2	49.6	24	1
123	2018 UE1	2.420	1095	02 Oct 2024	26.7	15.7	55	1
124	2018 LE1	2.423	1095	13 Aug 2024	27.5	10.9	55	1
125	2007 RO17	2.457	1050.54	12 Mar 2023	25.8	23.7	18	1
126	2016 FZ13	2.461	1095	17 Nov 2023	28.3	7.5	20	1
127	2014 HW	2.468	1023.04	30 Jun 2023	28.4	7.2	28	1
128	2015 TC25	2.488	1095	21 Dec 2024	29.3	4.7	44	2
129	2014 MZ17	2.510	1095	01 Jan 2023	24.1	51.9	47	2
130	2008 GM2	2.522	1095	16 Jan 2024	28.3	7.5	54	1
131	2017 BZ6	2.536	1095	14 Jul 2024	26.1	20.7	71	1
132	2012 WH	2.555	1078.02	04 Jun 2024	25.5	27.3	43	1
133	2017 QW1	2.560	1020.03	11 Jan 2023	26.2	19.7	36	1

134	2018 PR7	2.561	1095	30 Jun 2023	28.5	6.8	55	1
135	2017 QB35	2.579	1000.15	21 Dec 2024	29.3	4.7	33	1
136	2019 GE1	2.592	1095	03 Aug 2024	27	13.7	17	1
137	2014 UN114	2.598	922.45	01 Jan 2023	24.5	43.2	177	1
138	2005 QP11	2.603	1095	21 Jan 2023	26.4	18.0	53	1
139	2018 FH1	2.613	1095	04 Jul 2024	26.6	16.4	43	1
140	2012 PB20	2.626	1095	01 Jan 2023	24.9	35.9	45	1
141	2018 NX	2.634	1032.48	10 Jun 2023	27.7	9.9	28	1
142	2015 XC352	2.647	1092.40	05 Apr 2024	25.7	24.9	75	2
143	2016 TY55	2.702	1095	21 Dec 2024	26.9	14.3	44	1
144	2017 YS1	2.722	1095	11 May 2023	28.9	5.7	31	1
145	2019 LB1	2.726	1095	01 Nov 2024	27	13.7	61	1
146	2011 MQ3	2.765	1095	01 May 2023	24.8	37.6	71	1
147	YORP	2.776	1095	01 Apr 2023	22.7	99.0	533	5
148	2010 FY9	2.791	994.37	01 Jan 2023	26.7	15.7	22	1

Table B.14: Ranking of fuel-optimal transfers.

Appendix C. Fuel-optimal porkchops plots

Fuel-optimal porkchop plots for the 172 targets in Appendix A. The plots style has been simplified to favour readability, and common axes and color range have been adopted to ease comparison. The following conventions are used:

- x-axis: departure date; Range: Jan 1st, 2023–Dec 31st, 2024 (8401–9131 MJD2000);
- y-axis: time of flight; Range: 290–1095 days;
- Color code: fuel consumption; Range: 0.25–4.45 kg, same color code as in Fig. 12;
- Isolines step: 0.3 kg.

In all plots, the tick red line is the locus of time-optimal solutions, while the black dashed line (if present) indicates the available propellant mass isoline (2.8 kg).

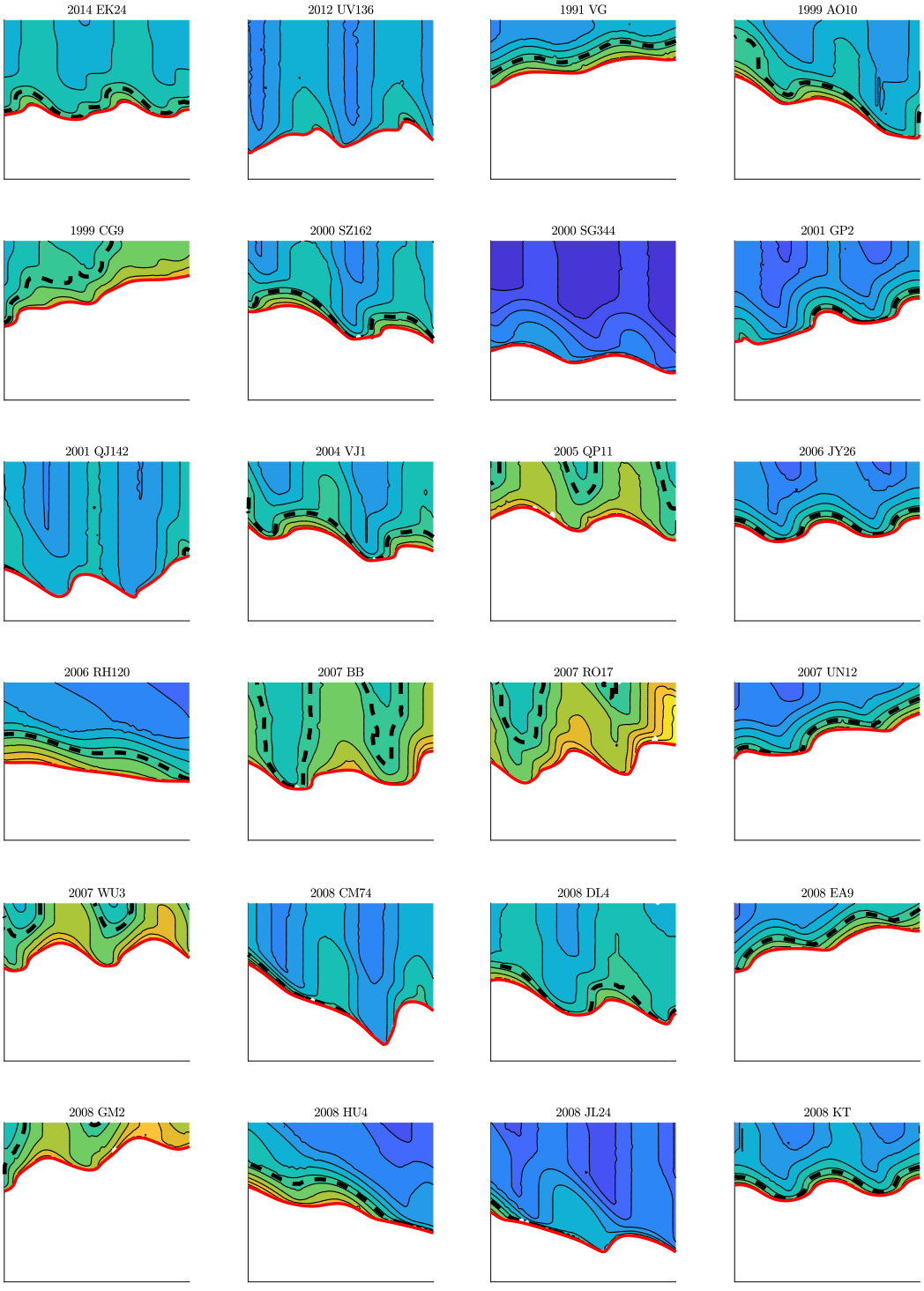
2014 EK24
2012 UV136
1991 VG
1999 AO10
1999 CG9
2000 SZ162
2000 SG344
2001 GP2
2001 QJ142
2004 VJ1
2005 QP11
2006 JY26
2006 RH120
2007 BB
2007 RO17
2007 UN12
2007 WU3
2008 CM74
2008 DL4
2008 EA9
2008 GM2
2008 HU4
2008 JL24
2008 KT

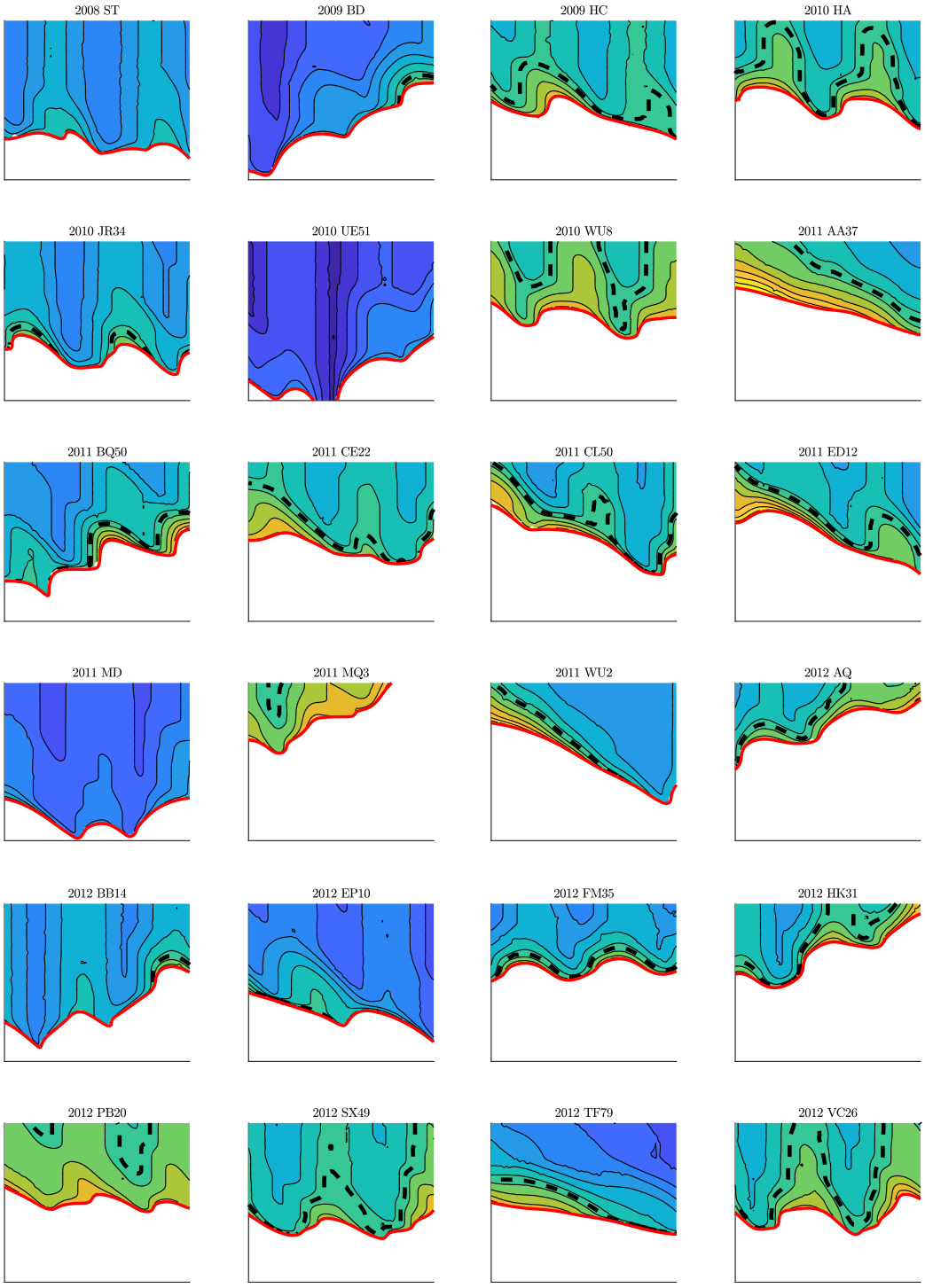
2008 ST
2009 BD
2009 HC
2010 HA
2010 JR34
2010 UE51
2010 WU8
2011 AA37
2011 BQ50
2011 CE22
2011 CL50
2011 ED12
2011 MD
2011 MQ3
2011 WU2
2012 AQ
2012 BB14
2012 EP10
2012 FM35
2012 HK31
2012 PB20
2012 SX49
2012 TF79
2012 VC26

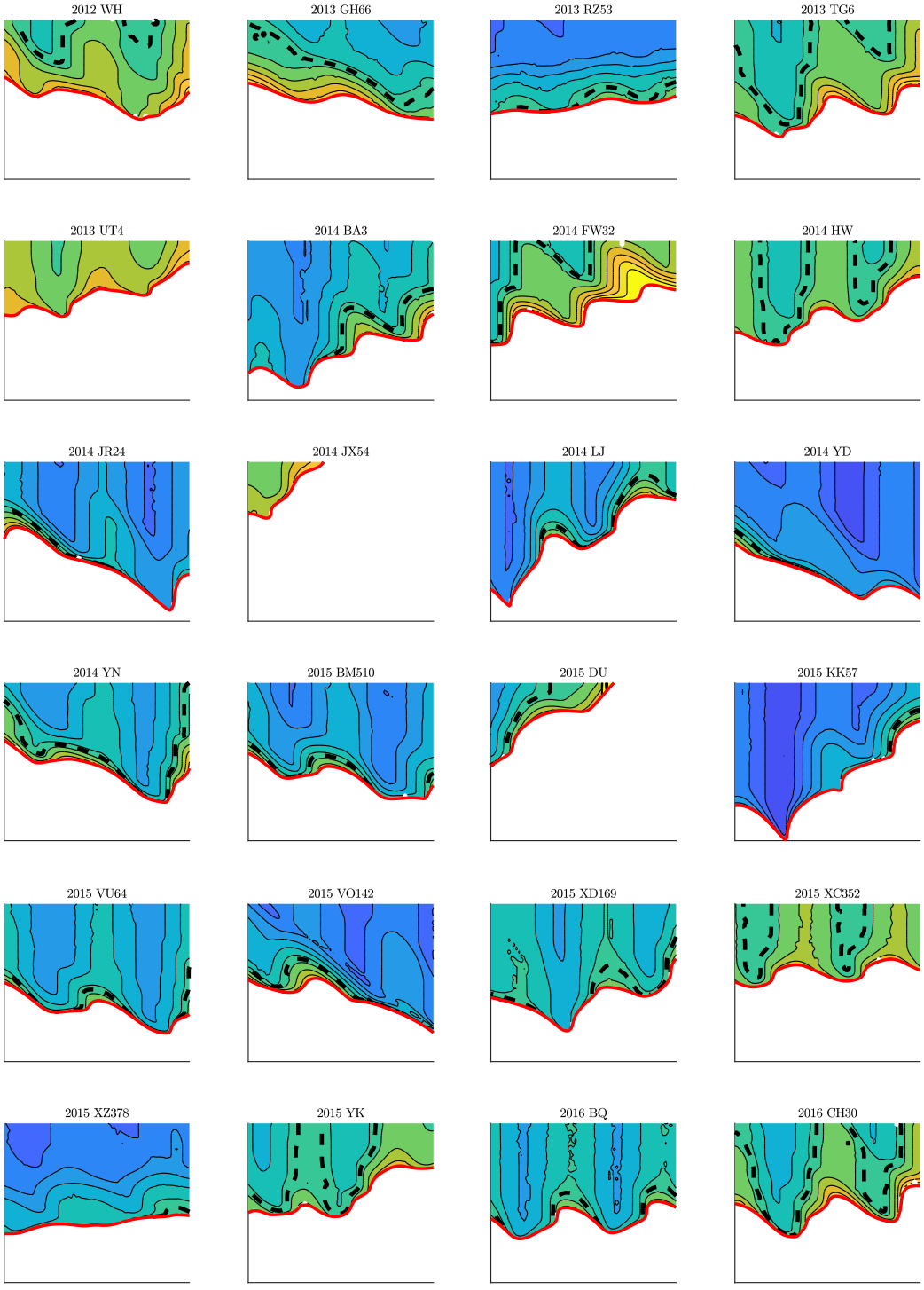
2012 WH
2013 GH66
2013 RZ53
2013 TG6
2013 UT4
2014 BA3
2014 FW32
2014 HW
2014 JR24
2014 JX54
2014 LJ
2014 YD
2014 YN
2015 BM510
2015 DU
2015 KK57
2015 VU64
2015 VO142
2015 XD169
2015 XC352
2015 XZ378
2015 YK
2016 BQ
2016 CH30

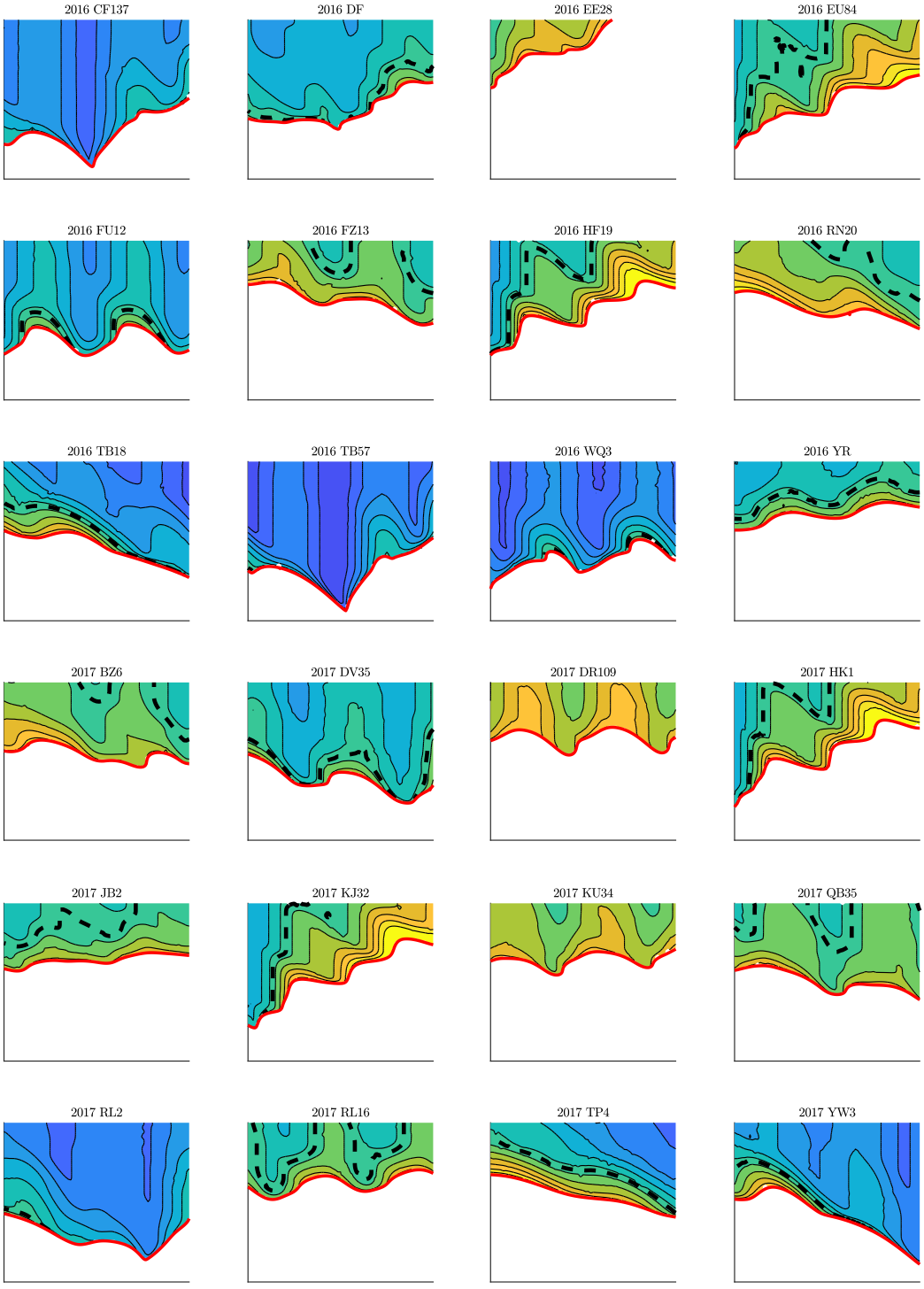
2016 CF137
2016 DF
2016 EE28
2016 EU84
2016 FU12
2016 FZ13
2016 HF19
2016 RN20
2016 TB18
2016 TB57
2016 WQ3
2016 YR
2017 BZ6
2017 DV35
2017 DR109
2017 HK1
2017 JB2
2017 KJ32
2017 KU34
2017 QB35
2017 RL2
2017 RL16
2017 TP4
2017 YW3

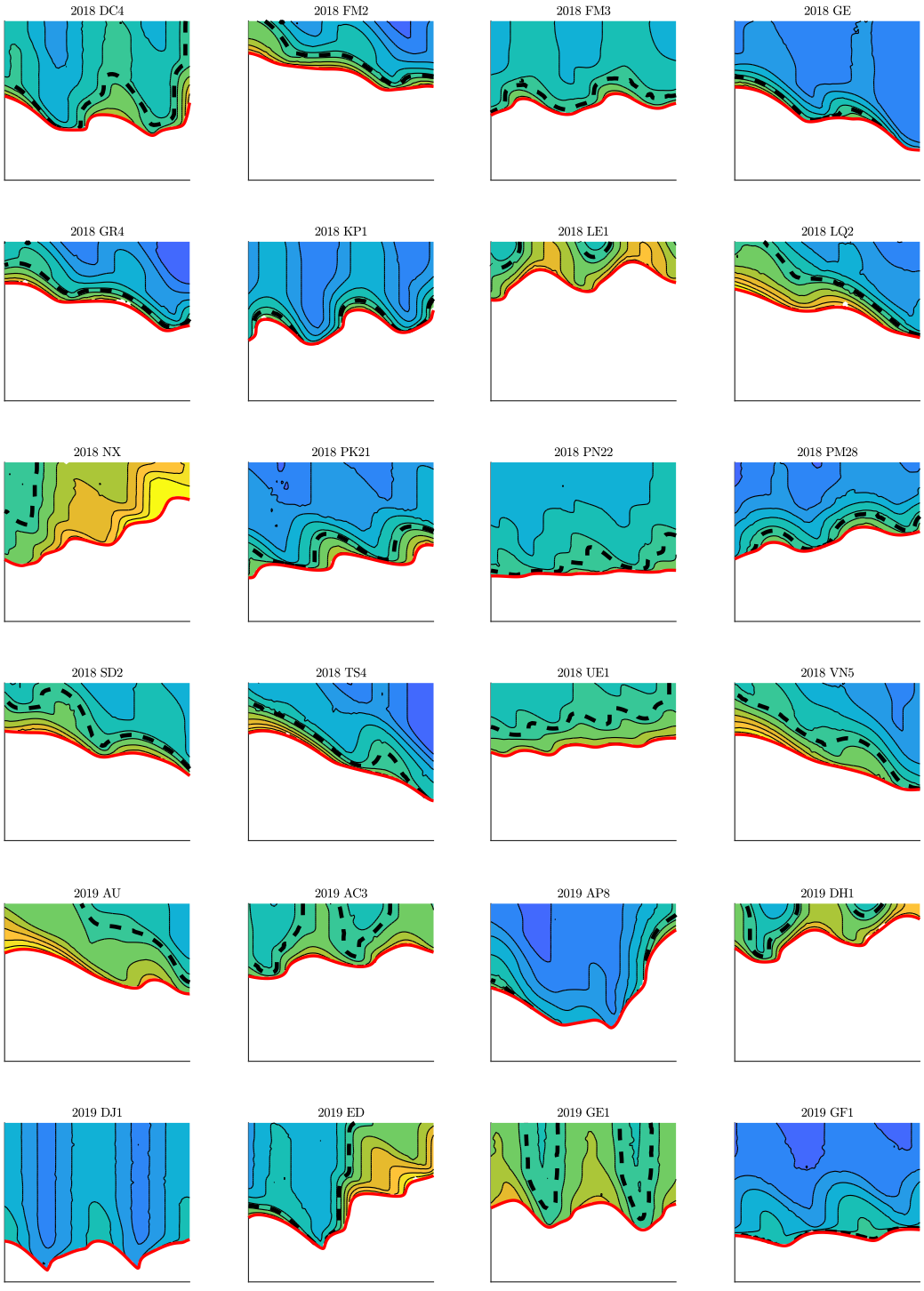
2018 DC4
2018 FM2
2018 FM3
2018 GE
2018 GR4
2018 KP1
2018 LE1
2018 LQ2
2018 NX
2018 PK21
2018 PN22
2018 PM28
2018 SD2
2018 TS4
2018 UE1
2018 VN5
2019 AU
2019 AC3
2019 AP8
2019 DH1
2019 DJ1
2019 ED
2019 GE1
2019 GF1

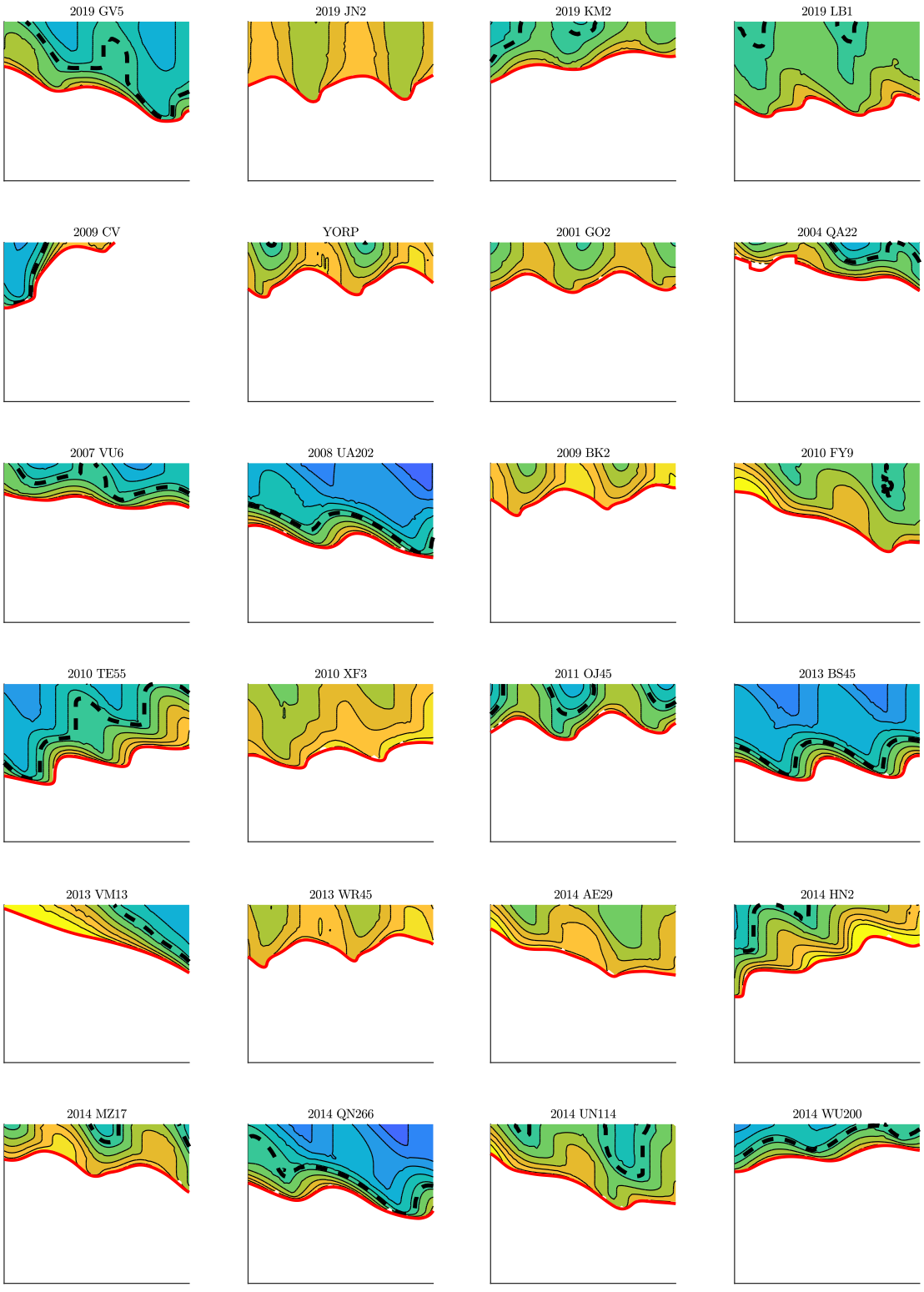
2019 GV5
2019 JN2
2019 KM2
2019 LB1
2009 CV
YORP
2001 GO2
2004 QA22
2007 VU6
2008 UA202
2009 BK2
2010 FY9
2010 TE55
2010 XF3
2011 OJ45
2013 BS45
2013 VM13
2013 WR45
2014 AE29
2014 HN2
2014 MZ17
2014 QN266
2014 UN114
2014 WU200

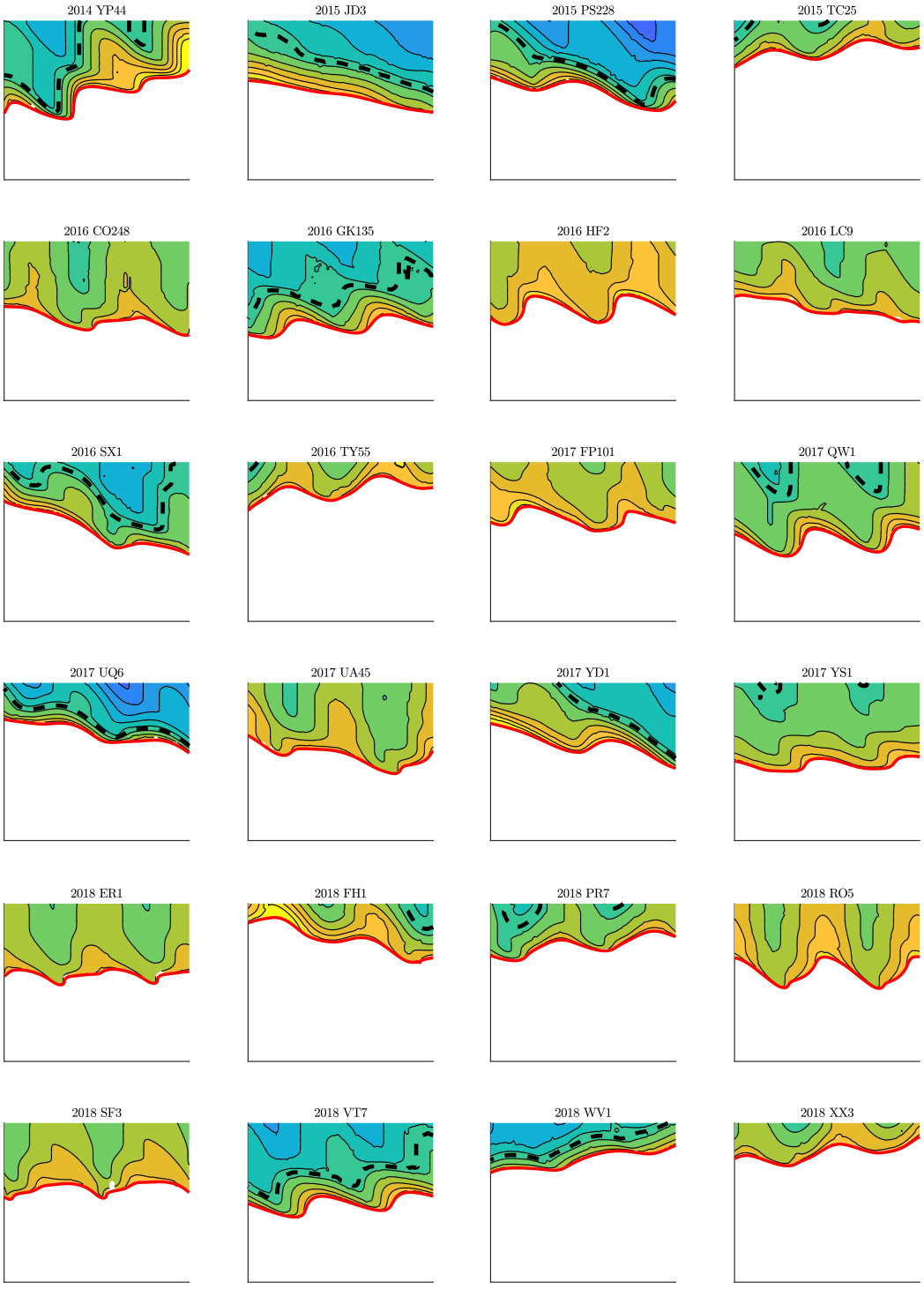
2014 YP44
2015 JD3
2015 PS228
2015 TC25
2016 CO248
2016 GK135
2016 HF2
2016 LC9
2016 SX1
2016 TY55
2017 FP101
2017 QW1
2017 UQ6
2017 UA45
2017 YD1
2017 YS1
2018 ER1
2018 FH1
2018 PR7
2018 RO5
2018 SF3
2018 VT7
2018 WV1
2018 XX3

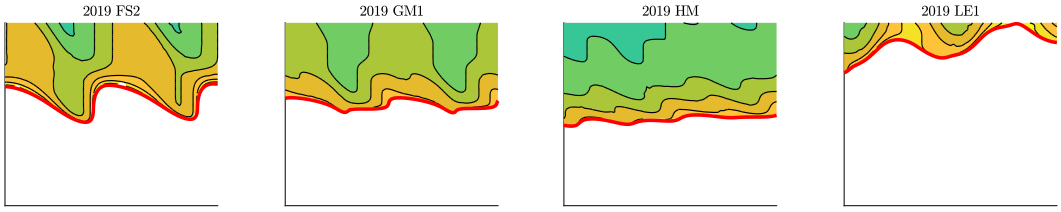
2019 FS2
2019 GM1
2019 HM
2019 LE1